1

LATTICE-BOLTZMANN MODELING OF MULTICOMPONENT SYSTEMS: AN INTRODUCTION

Ulf D. Schiller and Olga Kuksenok
Department of Materials Science and Engineering, Clemson University, Clemson, SC, USA

INTRODUCTION

The study of soft condensed matter is a rich and broad field that keeps engaging researchers from diverse backgrounds in science and engineering. Soft matter generally refers to materials whose characteristic energies, for example, the energy required for mechanical deformations, are on the order of the thermal energy at room temperature. Thermal fluctuations are thus a determining factor for the structure and properties of soft matter, and the characteristic behavior is governed by interactions at the "mesoscale," that is, at intermediate scales between the atomic and the macroscopic scale. Typical examples include colloidal and polymeric suspensions, liquid crystals, gels, and biological materials. Many soft matter systems are in a liquid state and their rheology and transport properties are of particular interest. While simple liquids usually exhibit Newtonian hydrodynamics, soft matter systems often show strongly nonlinear rheology such as shear thinning or shear thickening. This is due to the presence of the additional length scales in a multicomponent system that give rise to complex response characteristics, hence liquid soft matter systems are also referred to as "complex fluids."

Complex fluids are a challenge for theory because the interplay of different physics across a multitude of length scales means that the system typically cannot

Reviews in Computational Chemistry, First Edition. Edited by Abby L. Parrill and Kenny B. Lipkowitz.

be described by simple equations. Even if constitutive relations are known that allow, for example, a description at the hydrodynamic level, the nonlinear characteristics often make the system intractable. Computer simulations, on the other hand, are faced with the immense number of degrees of freedom in a liquid system. Fortunately, it is often not necessary to treat the dynamics of each individual degree of freedom. If a sufficient scale separation exists, the "fast" degrees of freedom can be averaged or "coarse-grained" into an effective representation that still captures the relevant dynamics on the scale of interest. The coarse-grained degrees of freedom then evolve on a mesoscale, and accordingly the computational methods are commonly called *mesoscopic methods*. One particular example that has gained considerable popularity in the soft matter domain is the lattice Boltzmann method (LBM) that we discuss in this chapter. We will focus on two particular classes of complex fluids, namely solid–fluid and fluid–fluid systems.

In solid–fluid systems, such as colloidal suspensions, the rheological properties are strongly influenced by hydrodynamic interactions (HI). HI refer to long-range correlations between the suspended particles that are mediated by the solvent, that is, perturbations of the flow (momentum) field that propagate through the solvent, where the transport of momentum is characterized by the viscosity of the fluid. A variety of mesoscopic methods have thus been developed to model the hydrodynamic momentum transport in a coarse-grained solvent. In contrast to particle-based mesoscopic methods, the LBM is a kinetic model where the fluid is represented by a set of mass distributions that evolve on a discrete lattice according to a highly simplified update rule. The LBM can be derived rigorously from kinetic theory and the solvent viscosity can be directly controlled through a single simulation parameter (without need for calibration). Moreover, thermal fluctuations can be incorporated in a systematic fashion that is consistent with the principles of statistical mechanics. The foundations of the LBM as they have been developed for single-phase fluids will be reviewed in the section "The Lattice Boltzmann Equation: A Modern Introduction." An excellent comprehensive review on lattice Boltzmann simulations of soft matter systems is given by Dünweg and Ladd.[1]

Flows of fluid–fluid multicomponent systems also occur in a variety of natural as well as technologically relevant processes, from ink-jet printing and processing of multicomponent polymer blends to multiphase flows of oil–water mixtures in a porous medium during enhanced oil recovery processes. Therefore, modeling of such flows is of interest for numerous applications. One of the major challenges in modeling the dynamics of multiphase fluids is tracking or capturing the position of the interface between the fluid components. The interface can be represented either as a sharp (infinitely thin) interface, or as a so-called diffuse (finite) interface, where the boundary between the phases is relatively wide (or diffuse) and is often described through the effective phase field as introduced below. The methods available to solve problems involving multiple fluids are often divided into the sharp-interface methods and diffuse-interface methods, respectively. A number of approaches (such as as boundary integral and boundary element methods)

can be used to track a sharp moving interface; in such methods, a grid undergoes deformation as the interface is deformed and re-meshing of the interface is typically required. Keeping track of the moving interface can be computationally expensive, especially for the cases where morphological transitions are of interest (such as phase separation between the components).

The multiphase LBM approach belongs to the class of diffusive interface methods.[2,3] An important advantage of these methods is that the interface does not need to be tracked, but the interfacial flows including dynamics of the phase separation are captured through the interactions between the different components. In this chapter, we focus on the free-energy lattice Boltzmann approach proposed by Swift et al.[4,5] and on practical application of this approach. This model was developed originally for both binary fluid and lattice-gas systems. The advantage of this approach is that the equilibrium distribution functions are defined based on the system's free energy, which also includes a gradient term defining an interfacial tension, as we show below. This allows one to define and vary the interfacial tension in these systems more easily than in other multiphase LBM approaches.

We first briefly comment on a few other multiphase LBM approaches, specifically on a color gradient method proposed by Gunstensen et al.[6] and a pseudopotential model by Shan and Chen.[7,8] The color gradient approach was the first multiphase LBM approach. In this method, instead of a single distribution function as, for example, defined for the single-component fluid, two-particle distribution functions were introduced for the first time: red and blue distribution functions for two different immiscible red and blue fluid phases. Local equilibrium distribution functions are defined by the local macroscopic parameters for each component, and are updated based on the color gradients during the "recoloring" step.[6] The phase separation in this approach is driven by the repulsive interactions based on the color gradient and momentum. In the Shan–Chen pseudo-potential model,[7,8] where non-local interactions were introduced, these interactions are controlled by the equation of state and result in the spontaneous phase separation between the components when the equation of state is appropriately chosen. The Shan–Chen model is currently one of the most commonly used multiphase LBM approaches. An excellent review comparing all these approaches for multiphase flows is given by Chen and Doolen.[9] A number of more recent reviews on multiphase LBM focus either on recent developments in LBM simulations of complex flows[10] or on more specific problems such as flow in a porous medium[11] or with heat transfer.[12]

In this chapter, we provide an introduction to both single-phase and a multiphase LBM and briefly comment on some of the recent developments of several key topics like the introduction of the multiple relaxation time collision operator into a multiphase LBM and possible strategies for minimizing spurious velocities. For more detailed information, we refer the reader to the respective original publications.

THE LATTICE BOLTZMANN EQUATION: A MODERN INTRODUCTION

The LBM describes a fluid system by a collection of particle distributions that move along discrete directions from site to site on a space-filling lattice. In the absence of external forces, the evolution of this system is given by the lattice Boltzmann equation

$$\bar{f}_i(\mathbf{x}+h\mathbf{c}_i,t+h)=\bar{f}_i^*(\mathbf{x},t)=\bar{f}_i(\mathbf{x},t)-\sum_j \Lambda_{ij}\left[\bar{f}_j(\mathbf{x},t)-f_j^{\mathrm{eq}}(\mathbf{x},t)\right] \quad [1]$$

where $\bar{f}_i(\mathbf{x},t)$ is a particle distribution at site $\mathbf{x}$ at time t associated with the discrete velocity direction $\mathbf{c}_i$, h is a time step, f_i^{eq} is a local equilibrium distribution, and Λ_{ij} is a collision matrix. The symbol $\bar{f}_i$ is used to distinguish the discrete distribution function $\bar{f}_i(\mathbf{x},t)$ from its continuum counterpart $f(\mathbf{x}, \mathbf{c}_i, t)$. The difference will become clear later in the derivation of the lattice Boltzmann equation. Equation [1] describes a two-stage update. In the first stage, the *collision step*, the distributions are locally updated according to the collision matrix Λ_{ij} resulting in post-collisional distributions $\bar{f}_i^*(\mathbf{x},t)$. In the second stage, the *streaming step*, the distributions $\bar{f}_i^*(\mathbf{x},t)$ move along the associated velocity direction from $\mathbf{x}$ to $\mathbf{x}+h\mathbf{c}_i$ to complete one time step h. The moments of the distribution functions are hydrodynamic variables, and it can be shown that on macroscopic time and length scales and in the incompressible limit, the Navier–Stokes equations are recovered, that is,

$$\frac{\partial\rho}{\partial t}+\frac{\partial\rho\mathbf{u}}{\partial\mathbf{r}}=0 \quad [2a]$$

$$\frac{\partial\rho\mathbf{u}}{\partial t}+\frac{\partial\rho\mathbf{u}\mathbf{u}}{\partial\mathbf{r}}=-\frac{\partial p}{\partial\mathbf{r}}+\eta\frac{\partial^2\mathbf{u}}{\partial\mathbf{r}^2} \quad [2b]$$

where $\rho(\mathbf{r}, t)$, $p(\mathbf{r}, t)$, and $\mathbf{u}(\mathbf{r}, t)$ are the density, pressure, and flow velocity of the fluid at position $\mathbf{r}$ and time t, and η is the Newtonian viscosity. The momentum flux is given by the stress tensor $\Pi=p\mathbf{I}+\rho\mathbf{u}\mathbf{u}-\eta\left[\nabla\mathbf{u}+(\nabla\mathbf{u})^t\right]$. While the connection between the lattice Boltzmann equation and the Navier–Stokes equation is typically established through the Chapman–Enskog expansion,[13] the lattice Boltzmann equation is in fact a fully discretized version of the Boltzmann equation. In the following sections we will show how the lattice Boltzmann equation can be systematically derived. We will clarify the approximations involved which are needed to understand the limits in which the LBM is valid and stable. However, readers who are more interested in the practical aspects of the LBM may skip the derivation and jump to the section on common lattice Boltzmann models.

A Brief History of the LBM

The LBM emerged some 30 years ago from the so-called lattice gas automata (LGA).[14–16] The LGA were a special class of cellular automata based on particles moving on a discrete lattice subject to certain collision rules. LGA were already used by Kadanoff and Swift,[17] and the HPP model named after Hardy, Pomeau, and de Pazzis[18] is widely referred to as the first LGA for fluid dynamics. However, since the HPP model is based on a square lattice, it lacks sufficient rotational symmetry and cannot reproduce the Navier–Stokes equation. This deficiency was overcome by Frisch et al.[19] by using a triangular lattice with hexagonal symmetry. The FHP model, named after Frisch, Hasslacher, and Pomeau, was the first LGA that could fully reproduce the Navier–Stokes equation in two dimensions. The direct extension of these models to three dimensions does not yield space-filling lattices with sufficient symmetry.[16] The first three-dimensional LGA was based on the projections of a four-dimensional face-centered hypercubic (FCHC) lattice and was actually published in 1986.[20] Already in these early stages it was realized that the symmetry of the lattice is essential for the macroscopic behavior, and the Navier–Stokes equation requires isotropy of tensors up to fourth rank.[14,15] The Navier–Stokes equation emerges from the LGA dynamics in the limit of small Mach number *Ma* and small Knudsen number *Kn*,[15,21] which is today routinely verified in terms of the Chapman–Enskog expansion.[13] An understanding of the symmetry requirements then lead to the development of the first multi-speed models that introduced additional velocity shells with speed-dependent weights.[16,20]

While LGA were easy to implement thanks to their Boolean nature, they were "plagued by several diseases."[16] Namely, the Boolean variables were subject to statistical noise and in order to recover fluid flows, a considerable amount of statistical averaging was required thus substantially limiting the efficiency of the method. Frisch et al.[15] were able to calculate the viscosity from linear response theory using ensemble-averaged variables, and McNamara and Zanetti[22] put forward the idea to use the ensemble-averaged populations to replace the Boolean occupation numbers as the dynamic variables, which finally led to the celebrated LBM. At first, the collision operator was derived from the collision rules of the underlying LGA microdynamics, until Higuera and Jimenez[23] linearized the resulting collision operator around the equilibrium distribution. This simplified the collision step substantially and established an interpretation of the LBM in terms of kinetic theory, which subsequently led to the adoption of the single relaxation time approximation known as the Bhatnagar–Gross–Krook (BGK) collision operator.[24–26] The lattice BGK collision operator is still one of the most widely used collision models in the LBM as described later in the section on common lattice Boltzmann models. In an overview of various lattice models, Qian et al.[27] coined the nomenclature D*n*Q*m* for *n*-dimensional lattice models with *m* velocities that is now commonly used as a standard classification. The LBM has emerged as a powerful tool to simulate hydrodynamic phenomena governed by the Navier–Stokes equation. Perhaps the main reason for its success is that, while the

Navier-Stokes equation is a nonlinear and nonlocal partial differential equation, in the lattice Boltzmann equation the nonlocality becomes linear (streaming step) and the nonlinearity becomes local (collision step).[28]

The essential elements of the LBM are the local equilibrium distribution and the linearized collision operator. Whereas the BGK collision operator fixes the Prandtl number $Pr = \nu/\alpha$ (the ratio of the kinematic viscosity ν and the thermal diffusivity α) and the ratio of the bulk and shear viscosities, these limitations can be overcome by using a multi-relaxation-time (MRT) collision operator.[29–31] The additional relaxation parameters in the MRT model can be used to tune the macroscopic behavior and improve stability by controlling the relaxation of higher moments independently.[32] As we will see later, the MRT model provides a general formalism for the LBM that includes LBGK and other collision models as special cases. A significant contribution to the success of the LBM was the development of a systematic *a priori* derivation of the lattice Boltzmann equation from the continuous Boltzmann equation.[33–36] The LBM is thus not just a Navier–Stokes solver but a discrete kinetic model that, in principle, is capable of simulating phenomena beyond the Navier–Stokes equation[28] and the *a priori* derivations pave the way to the development of complex fluid models including multiphase systems. An important consequence of the truncation of the velocity space is that the LBM does not guarantee an *H*-theorem.[37] Karlin and coworkers[38–40] have addressed this deficiency and developed the entropic lattice Boltzmann models, where the equilibrium distribution is derived from entropy functions and the collision operator is constructed such that a discrete *H*-theorem is satisfied. The entropic LBM improves stability and can reduce the computational costs of lattice Boltzmann simulations of high Reynolds number flows.[41,42] Moreover, the entropy functions establish a systematic link to the underlying statistical mechanics of the LBM. This has subsequently inspired the development of fluctuating lattice Boltzmann models.[43–45] In recent years, further progress has been made in developing more stable lattice Boltzmann models by systematically expanding the Hermitian representation of the discrete velocity space.[46–48]

The LBM is inherently a multiscale method and is thus perfectly suited to model complex fluids whose transport properties are governed by an interplay of interactions at different length and time scales.[1] Pioneering applications in soft matter were performed by Ladd and coworkers[49–51] who used the LBM to model colloidal suspensions. On an alternative route, Dünweg and coworkers[52–54] developed a particle–fluid coupling that allows one to simulate suspended molecules with internal degrees of freedom such as polymer chains. Finally, another important development are the LBMs for multicomponent and multiphase fluids. The first multicomponent models were based on "colored" components that undergo specific collisions leading to phase separation.[16] In their seminal work, Shan and Chen[7,8] modeled the nonlocal interactions by explicit interaction potentials. The Shan–Chen model is still one of the most widely used multicomponent lattice Boltzmann models. An alternative model was developed by Yeomans and coworkers[4,5] where the interactions are systematically derived from a free-energy approach; we will

describe this approach in detail in the Section "LBM for Multiphase Fluids." The resulting equilibrium distribution is consistent with the thermodynamics of the system. Due to the incompressible limit of the original LBM, however, the multiphase models are typically restricted to small density contrasts between the phases and tend to suffer from spurious currents, a topic that will be described later in this tutorial. The development of improved multiphase models remains an active research area,[55] and in this review we will highlight some of the more recent efforts and applications.

The Lattice Boltzmann Equation

Continuum Kinetic Theory In continuum kinetic theory, the one-particle distribution function is described by the Boltzmann equation[56]

$$\left(\frac{\partial}{\partial t}+\mathbf{v}\cdot\frac{\partial}{\partial \mathbf{x}}+\mathbf{a}\cdot\frac{\partial}{\partial \mathbf{v}}\right)f(\mathbf{r},\mathbf{v},t)=\mathcal{C}[f(\mathbf{r},\mathbf{v},t)] \qquad [3]$$

where $f(\mathbf{r}, \mathbf{v}, t)$ is the one-particle distribution function at position $\mathbf{r}$, velocity $\mathbf{v}$, and time t, subject to an acceleration $\mathbf{a}$. The collisional change on the right-hand side is written in terms of the nonlinear collision operator $\mathcal{C}$. The equilibrium solution of the Boltzmann equation [3] is the Maxwell–Boltzmann distribution[57,58]

$$f^{\mathrm{eq}}(\mathbf{v})=\rho\left(\frac{m}{2\pi kT}\right)^{\frac{3}{2}}\exp\left[-\frac{m(\mathbf{v}-\mathbf{u})^2}{2kT}\right] \qquad [4]$$

Since the equilibrium distribution is a collisional invariant, that is, $\mathcal{C}[f^{\mathrm{eq}}]=0$, the collision operator can be linearized[24,59]

$$\mathcal{C}[f]\approx\left.\frac{\delta\mathcal{C}}{\delta f}\right|_{f^{\mathrm{eq}}}(f-f^{\mathrm{eq}})=\mathcal{L}(f-f^{\mathrm{eq}}) \qquad [5]$$

The simplest form of the linearized collision operator $\mathcal{L}$ is the BGK approximation introduced by Bhatnagar et al.[24]

$$\mathcal{L}_{\mathrm{BGK}}(f-f^{\mathrm{eq}})=-\frac{1}{\tau}(f-f^{\mathrm{eq}}) \qquad [6]$$

which is also referred to as a single relaxation time model because all variables have the same relaxation time τ.

The hydrodynamic variables are the moments of the distribution function f given by

$$\rho(\mathbf{r},t)=\int f(\mathbf{r},\mathbf{v},t)\,d\mathbf{v} \qquad [7a]$$

$$\rho(\mathbf{r},t)\mathbf{u}(\mathbf{r},t) = \int \mathbf{v} f(\mathbf{r},\mathbf{v},t)\, d\mathbf{v} \qquad [7b]$$

$$\Pi(\mathbf{r},t) - p\mathsf{I} = \int \left(\mathbf{v}\otimes\mathbf{v} - c_s^2\mathsf{I}\right) f(\mathbf{r},\mathbf{v},t)\, d\mathbf{v} \qquad [7c]$$

where $c_s = \sqrt{kT/m}$ is the speed of sound. Only the first 10 moments are included in the Navier–Stokes equation that describes the hydrodynamics on the macroscopic scale

$$\frac{\partial \rho}{\partial t} + \frac{\partial \rho \mathbf{u}}{\partial \mathbf{r}} = 0 \qquad [8a]$$

$$\frac{\partial \rho \mathbf{u}}{\partial t} + \frac{\partial \Pi}{\partial \mathbf{r}} = \rho \mathbf{a} \qquad [8b]$$

The moment integrals can be generally written as

$$\mathsf{a}^{(n)}(\mathbf{r},t) = \int \mathsf{H}^{(n)}(\mathbf{v}) f(\mathbf{r},\mathbf{v},t)\, d\mathbf{v} \qquad [9]$$

where $\mathsf{H}^{(n)}$ are Hermite tensor polynomials,[36,60] which form an orthogonal basis of the space $\mathcal{H}$ of square-integrable functions with the scalar product

$$\langle g|h\rangle = \int g(\mathbf{v}) h(\mathbf{v}) \omega(\mathbf{v})\, d\mathbf{v} \qquad [10]$$

where the weight function $\omega(\mathbf{v}) = (2\pi kT/m)^{-3/2} \exp[-m\mathbf{v}^2/2kT]$. The norm of the Hermite tensor polynomials is

$$\int \left[\mathsf{H}^{(n)}_{\alpha_1\ldots\alpha_n}(\mathbf{v})\right]^2 \omega(\mathbf{v})\, d\mathbf{v} = \frac{1}{n_x! n_y! n_z!} \qquad [11]$$

where n_k is the number of occurrences of the component $k \in \{x,y,z\}$ in $\alpha_1 \ldots \alpha_n$ and $n_x + n_y + n_z = n$.

The distribution function f may thus be written as a series[60,61]

$$f(\mathbf{r},\mathbf{v},t) = \omega(\mathbf{v}) \sum_{n=0}^{\infty} \sum_{\alpha_1\ldots\alpha_n} \frac{1}{n_x! n_y! n_z!} \mathsf{a}^{(n)}_{\alpha_1\ldots\alpha_n}(\mathbf{r},t) \mathsf{H}^{(n)}_{\alpha_1\ldots\alpha_n}(\mathbf{v}) \qquad [12]$$

where the second summation runs over all combinations of indices with $n_x + n_y + n_z = n$. This Hermitian representation is the starting point for a systematic discretization of the Boltzmann equation that leads to the lattice Boltzmann equation.

Discrete Velocity Models The first step in discretizing the continuous Boltzmann equation is a projection of the distribution function onto a subspace of $\mathcal{H}$ in terms of a finite orthogonal basis. This is usually achieved by truncating the Hermite expansion, Eq. [12], at some order N:

$$f^N(\mathbf{r},\mathbf{v},t) = \omega(\mathbf{v})\sum_{n=0}^{N}\sum_{\alpha_1\ldots\alpha_n}\frac{1}{n_x!n_y!n_z!}\mathsf{a}^{(n)}_{\alpha_1\ldots\alpha_n}(\mathbf{r},t)\mathsf{H}^{(n)}_{\alpha_1\ldots\alpha_n}(\mathbf{v}) \qquad [13]$$

If the truncation is chosen such that the orthogonality of the Hermite tensor polynomials is preserved, the projection does not change the expansion coefficients up to order N:

$$\mathsf{a}^{(n)}(\mathbf{r},t) = \int \mathsf{H}^{(n)}(\mathbf{v})f(\mathbf{r},\mathbf{v},t)\,d\mathbf{v} = \int \mathsf{H}^{(n)}(\mathbf{v})f^N(\mathbf{r},\mathbf{v},t)\,d\mathbf{v}, \quad n \le N \qquad [14]$$

The hydrodynamic moments can thus be written

$$\mathsf{a}^{(n)}(\mathbf{r},t) = \int \mathsf{H}^{(n)}(\mathbf{v})f^N(\mathbf{r},\mathbf{v},t)\,d\mathbf{v} = \int \omega(\mathbf{v})\frac{H^{(n)}(\mathbf{v})f^N(\mathbf{r},\mathbf{v},t)}{\omega(\mathbf{v})} \qquad [15]$$

Since $\mathsf{H}^{(n)}f^N/\omega$ with $n \le N$ is a polynomial of degree of at most $2N$, the integral can be evaluated using a Gauss–Hermite quadrature[36]

$$\mathsf{a}^{(n)}(\mathbf{r},t) = \sum_i w_i \frac{\mathsf{H}^{(n)}(\mathbf{c}_i)f^N(\mathbf{r},\mathbf{c}_i,t)}{\omega(\mathbf{c}_i)} = \sum_i f_i(\mathbf{r},t)\mathsf{H}^{(n)}(\mathbf{c}_i) \qquad [16]$$

where $\mathbf{c}_i$ and w_i are the nodes and weights of the quadrature and $f_i(\mathbf{r}, t)$ is the distribution associated with the discrete velocity $\mathbf{c}_i$:

$$f_i(\mathbf{r},t) = \frac{w_i f^N(\mathbf{r},\mathbf{c}_i,t)}{\omega(\mathbf{c}_i)} \qquad [17]$$

The equilibrium distribution can be expanded in the same way to give

$$f_i^{\mathrm{eq}}(\mathbf{r},t) = w_i\sum_{n=0}^{N}\sum_{\alpha_1\ldots\alpha_n}\frac{\mathsf{a}^{\mathrm{eq},(n)}_{\alpha_1\ldots\alpha_n}(\mathbf{r},t)}{n_x!n_y!n_z!}\mathsf{H}^{(n)}_{\alpha_1\ldots\alpha_n(\mathbf{c}_i)} \qquad [18]$$

The projection of the Boltzmann equation onto the finite subspace is written in the form

$$\left(\frac{\partial}{\partial t} + \mathbf{c}_i\cdot\frac{\partial}{\partial \mathbf{r}}\right)f_i(\mathbf{r},t) = -\Omega_{ij}\left[f_j(\mathbf{r},t) - f_j^{\mathrm{eq}}(\mathbf{r},t)\right] + G_i \qquad [19]$$

where Ω_{ij} is a discrete collision matrix, and the force term G_i corresponds to the projection of the acceleration term $-\mathbf{a}\cdot\nabla_{\mathbf{v}}f$.

$$\sum_i G_i = 0 \quad \sum_i \mathbf{c}_i G_i = \rho\mathbf{a} \quad \sum_i \mathbf{c}_i\mathbf{c}_i G_i = \rho(\mathbf{a}\otimes\mathbf{u} + \mathbf{u}\otimes\mathbf{a}) \qquad [20]$$

The discrete Boltzmann equation [19] is also referred to as a discrete velocity model (DVM).[62,63]

To evaluate hydrodynamic moments up to order N, the Gauss–Hermite quadrature needs to have a degree $d \geq 2N$. For a second-order approximation, we thus need a quadrature of degree $d \geq 4$. The construction of three-dimensional quadratures is discussed in more detail in Ref. 36. Our naming of the lattices follows the classification scheme introduced by Qian[27] where a DnQm model denotes an n dimensional model with m velocity vectors. Several of the most common lattice Boltzmann lattices, for example, D2Q9, D3Q15, and D3Q19, stem from degree-5 quadratures and are listed in Table 1. It should be noted that not all quadratures produce discrete velocities that correspond to a space-filling lattice. Vice-versa, there are valid lattice models (such as D3Q13) whose discrete velocities do not necessarily correspond to the nodes of a Gauss–Hermite quadrature.[30,36] One of the most common three-dimensional lattice is the D3Q19, which is illustrated in Figure 1. Its (dimensionless) velocity vectors $\mathbf{c}_i$ are given below that figure.

An important condition of the discrete velocities that is automatically guaranteed by the quadratures is the isotropy of lattice tensors up to the degree of the quadrature[65]

$$T^{(n)} = \sum_i w_i \mathbf{c}_i \ldots \mathbf{c}_i = \begin{cases} 0 & n \text{ odd} \\ \delta^{(n)} & n \text{ even} \end{cases} \quad \forall n \leq m \qquad [21]$$

As was noted by Philippi and coworkers,[46] the essential relation between the finite Hermite subspace and the discrete velocities $\mathbf{c}_i$ is the preservation of the scalar product

$$\int \mathsf{H}^{(n)}(\mathbf{v})\mathsf{H}^{(m)}(\mathbf{v})\omega(\mathbf{v})d\mathbf{v} = \sum_i w_i \mathsf{H}^{(n)}(a_s\mathbf{c}_i)\mathsf{H}^{(m)}(a_s\mathbf{c}_i) \qquad [22]$$

where a_s is a scaling factor. The connection between the conditions [21] and [22] are the orthogonality and the recurrence relations of the Hermite tensor polynomials. For a prescribed set of discrete velocities, both equations lead to a set of equations that can be solved for the weights w_i and the scaling factor a_s (B. Dünweg, personal communication).[46,66] This procedure is sometimes referred to as "quadrature with prescribed abscissae" and has been used to produce lattices such as D2V17 and D2V37, which are constructed by sequentially filling the

TABLE 1 Gauss–Hermite Quadratures of Degree 5 in Different Dimensions and the Corresponding Lattice Boltzmann Models.

Quadrature	Lattice	q	b_q	w_q	$\mathbf{c}_q$
$E^3_{1,5}$	D1Q3	0	1	$\frac{2}{3}$	0
		1	2	$\frac{1}{6}$	$\pm\sqrt{3}$
$E^9_{2,5}$	D2Q9	0	1	$\frac{4}{9}$	(0,0)
		1	4	$\frac{1}{9}$	$(\pm\sqrt{3},0),\ (0,\pm\sqrt{3})$
		2	4	$\frac{1}{36}$	$(\pm\sqrt{3},\pm\sqrt{3})$
$E^{15}_{3,5}$	D3Q15	0	1	$\frac{2}{9}$	(0,0,0)
		1	6	$\frac{1}{9}$	$(\pm\sqrt{3},0,0),\ (0,\pm\sqrt{3},0),\ (0,0,\sqrt{3})$
		3	8	$\frac{1}{72}$	$(\pm\sqrt{3},\pm\sqrt{3},\pm\sqrt{3})$
$E^{19}_{3,5}$	D3Q19	0	1	$\frac{1}{3}$	(0,0,0)
		1	6	$\frac{1}{18}$	$(\pm\sqrt{3},0,0),\ (0,\pm\sqrt{3},0),\ (0,0,\sqrt{3})$
		2	12	$\frac{1}{36}$	$(\pm\sqrt{3},\pm\sqrt{3},0),\ (\pm\sqrt{3},0,\pm\sqrt{3}),$ $(0,\pm\sqrt{3},\pm\sqrt{3})$
$E^{27}_{3,5}$	D3Q27	0	1	$\frac{8}{27}$	(0,0,0)
		1	6	$\frac{2}{27}$	$(\pm\sqrt{3},0,0),\ (0,\pm\sqrt{3},0),\ (0,0,\sqrt{3})$
		2	12	$\frac{1}{54}$	$(\pm\sqrt{3},\pm\sqrt{3},0),\ (\pm\sqrt{3},0,\pm\sqrt{3}),$ $(0,\pm\sqrt{3},\pm\sqrt{3})$
		3	8	$\frac{1}{216}$	$(\pm\sqrt{3},\pm\sqrt{3},\pm\sqrt{3})$

Following Shan et al.,[36] the naming convention $E^n_{D,d}$ denotes a degree-d quadrature in D dimensions with n abscissae. The vectors $\mathbf{c}_q$ with the same value of $q = \|\mathbf{c}_i\|^2/3$ form a symmetry class within which the weight w_q does not vary. By scaling the $\mathbf{c}_q$ with $a_s = \sqrt{3}$, sublattices of the standard cubic lattice are obtained. *Source*: reproduced from Ref. 64.

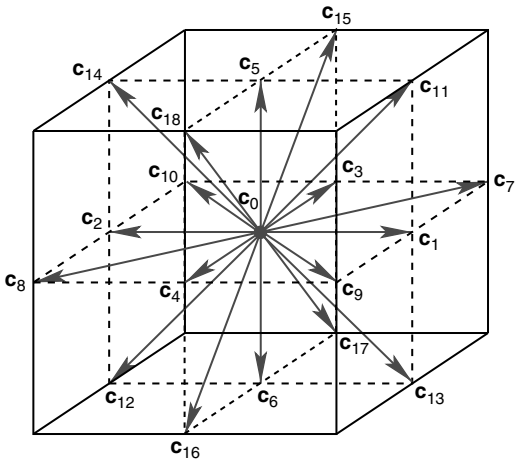

$$C = (\mathbf{c}_0\ \mathbf{c}_1\ \mathbf{c}_2\ \mathbf{c}_3\ \mathbf{c}_4\ \mathbf{c}_5\ \mathbf{c}_6\ \mathbf{c}_7\ \mathbf{c}_8\ \mathbf{c}_9\ \mathbf{c}_{10}\ \mathbf{c}_{11}\ \mathbf{c}_{12}\ \mathbf{c}_{13}\ \mathbf{c}_{14}\ \mathbf{c}_{15}\ \mathbf{c}_{16}\ \mathbf{c}_{17}\ \mathbf{c}_{18})$$
$$= \begin{pmatrix} 0 & 1 & -1 & 0 & 0 & 0 & 0 & 1 & -1 & 1 & -1 & 1 & -1 & 1 & -1 & 0 & 0 & 0 & 0 \\ 0 & 0 & 0 & 1 & -1 & 0 & 0 & 1 & -1 & -1 & 1 & 0 & 0 & 0 & 0 & 1 & -1 & 1 & -1 \\ 0 & 0 & 0 & 0 & 0 & 1 & -1 & 0 & 0 & 0 & 0 & 1 & -1 & -1 & 1 & 1 & -1 & -1 & 1 \end{pmatrix}$$

FIGURE 1 Illustration of the D3Q19 model. It uses 19 velocity vectors connecting the lattice sites: 6 links to the nearest neighbors, 12 links to the next nearest neighbors, and one zero velocity associated with a resting distribution. The vectors $\mathbf{c}_i$ are obtained by multiplying the columns of C by $a_s a/h$. Note that the order of the vectors is arbitrary.

Cartesian space around a lattice site[46] and are distinct from the DnQm quadrature lattices.

It is worth noting that the basis of the Hermite subspace needs not necessarily correspond to a strict truncation at a given order but can include partial sets of tensor polynomials at higher orders. For example, the D2Q9 lattice, which emerges from a second-order truncation including the first six tensor polynomials $\mathsf{H}^{(0)}$, $\mathsf{H}^{(1)}_x$, $\mathsf{H}^{(1)}_y$, $\mathsf{H}^{(2)}_{xx}$, $\mathsf{H}^{(2)}_{xy}$, and $\mathsf{H}^{(2)}_{yy}$, can be extended by including the three additional tensor polynomials $\mathsf{H}^{(3)}_{xxy}$, $\mathsf{H}^{(3)}_{xyy}$, and $\mathsf{H}^{(4)}_{xxyy}$ from the Cartesian product of the one-dimensional second-order sets.[67] The extension of the basis can improve the accuracy with which the nonequilibrium hydrodynamic moments are retrieved, and models that use the extended basis (such as MRT) are commonly observed to yield better accuracy and stability.[32,68] For this reason, it is crucial to use an equilibrium projection that is consistent with the Hermitian basis, for example, for the D2Q9 model the expanded equilibrium distribution reads

$$f_i^{\mathrm{eq}} = w_i \rho \left[1 + \frac{\mathbf{u}\cdot\mathbf{c}_i}{c_s^2}, + \frac{\mathbf{uu} : \left(\mathbf{c}_i\mathbf{c}_i - c_s^2\mathbf{I}\right)}{2\,c_s^4} + \frac{u_x^2 u_y \left(c_{ix}^2 - c_s^2\right) c_{iy}}{2\,c_s^6} + \frac{u_x\, u_y^2 \left(c_{iy}^2 - c_s^2\right) c_{ix}}{2\,c_s^6} + \frac{u_x^2\, u_y^2 \left(c_{ix}^2 - c_s^2\right)\left(c_{iy}^2 - c_s^2\right)}{4\,c_s^8} \right] \quad [23]$$

The procedures for velocity discretization described in this subsection are at the heart of the LBM. They are critical for deriving higher-order lattices required for applications such as thermal flows[47,66] For a more detailed discussion of the velocity discretization, we refer the reader to Refs. 36 and 46.

Space–Time Discretization The standard approach to space–time discretization of the discrete Boltzmann equation is integration along the characteristic and using the trapezium rule to evaluate the integral of the collision term.[33,34,69] More recently, it was pointed out by Dellar[70] that the discrete Boltzmann equation can also be integrated using Strang splitting. The discrete Boltzmann equation can be written in terms of operators[70,71]

$$\partial_t f_i(\mathbf{x}, t) = (\mathcal{S} + \mathcal{C} + \mathcal{F}) f_i(\mathbf{x}, t) \quad [24]$$

where the streaming, collision, and forcing terms are, respectively,

$$\mathcal{S} f_i = -\mathbf{c}_i \cdot \frac{\partial}{\partial \mathbf{x}} f_i \quad [25a]$$

$$\mathcal{C} f_i = -\sum_j \Omega_{ij} \left[f_j - f_j^{\mathrm{eq}} \right] \quad [25b]$$

$$\mathcal{F} f_i = G_i \quad [25c]$$

The streaming part can be integrated along the characteristic over a time step h:

$$\int_0^h \frac{d}{dh'} f_i(\mathbf{x} + h'\mathbf{c}_i, t + h') dh' = f_i(\mathbf{x} + h\mathbf{c}_i, t + h) - f_i(\mathbf{x}, t) = 0 \quad [26]$$

to obtain a discrete streaming step

$$f_i(\mathbf{x} + h\mathbf{c}_i, t + h) = \mathsf{S} f_i(\mathbf{x} + h\mathbf{c}_i, t) = f_i(\mathbf{x}, t) \quad [27]$$

The collision and the forcing term act locally and can be written in the form

$$\partial_t \mathbf{f} = -\Omega[\mathbf{f} - \mathbf{f}^{\mathrm{eq}}] + \mathbf{G} \tag{28}$$

where we have introduced the vector notation $\mathbf{f} = (f_0, f_1, \ldots, f_q)^T$ and $\mathbf{G} = (G_0, G_1, \ldots, G_q)^T$. Applying the Crank–Nicolson rule, we obtain an $O(h^3)$ approximation[70,72]

$$\begin{aligned} \mathbf{f}(t+h) - \mathbf{f}(t) = &-\frac{h}{2}\Omega[\mathbf{f}(t+h) - \mathbf{f}^{\mathrm{eq}}(t+h) + \mathbf{f}(t) - \mathbf{f}^{\mathrm{eq}}(t)] \\ &+ \frac{h}{2}[\mathbf{G}(t+h) + \mathbf{G}(t)] \end{aligned} \tag{29}$$

that leads to the discrete collision step

$$\begin{aligned} \mathbf{f}(t+h) = \mathsf{C}\mathbf{f}(t) = \mathbf{f}(t) &- \left(\mathsf{I} + \frac{h}{2}\Omega\right)^{-1} h\Omega\left[\mathbf{f}(t) - \frac{1}{2}(\mathbf{f}^{\mathrm{eq}}(t+h) + \mathbf{f}^{\mathrm{eq}}(t))\right] \\ &+ \left(\mathsf{I} + \frac{h}{2}\Omega\right)^{-1} \frac{h}{2}[\mathbf{G}(t+h) + \mathbf{G}(t)] \end{aligned} \tag{30}$$

For a second-order accurate approximation, we have to employ operator splitting in the form

$$f_i(\mathbf{x}, t+h) = \mathsf{C}^{1/2}\mathsf{S}\mathsf{C}^{1/2} f_i(\mathbf{x}, t) \tag{31}$$

and after n time steps

$$f_i(\mathbf{x}, t+h) = \left[\mathsf{C}^{1/2}\mathsf{S}\mathsf{C}^{1/2}\right]^n f_i(\mathbf{x}, t) = \mathsf{C}^{1/2}[\mathsf{S}\mathsf{C}]^n \mathsf{C}^{-1/2} f_i(\mathbf{x}, t) \tag{32}$$

The square root of the collision operator can be approximated by $\mathsf{C}^{1/2} = \frac{1}{2}(\mathsf{I} + \mathsf{C})$ such that

$$\begin{aligned} \mathsf{C}^{1/2}\bar{\mathbf{f}}(t) &= \left(\mathsf{I} + \frac{h}{2}\Omega\right)^{-1}\left[\bar{\mathbf{f}}(t) + \frac{h}{4}\Omega(\mathbf{f}^{\mathrm{eq}}(t+h) + \mathbf{f}^{\mathrm{eq}}(t)) + \frac{h}{4}(\mathbf{G}(t+h) + \mathbf{G}(t))\right] \\ &\approx \left(\mathsf{I} + \frac{h}{2}\Omega\right)^{-1}\left[\bar{\mathbf{f}}(t) + \frac{h}{2}\Omega\mathbf{f}^{\mathrm{eq}}(t) + \frac{h}{2}\mathbf{G}(t)\right] \end{aligned} \tag{33}$$

and $\mathsf{C}^{-1/2}$ is taken to be the exact inverse of Eq. [39]:

$$\begin{aligned}\mathsf{C}^{-1/2}\mathbf{f}(t) &= \left(\mathsf{I}+\frac{h}{2}\Omega\right)\mathbf{f}(t)-\frac{h}{4}\Omega(\mathbf{f}^{\mathrm{eq}}(t+h)+\mathbf{f}^{\mathrm{eq}}(t))-\frac{h}{4}(\mathbf{G}(t+h)+\mathbf{G}(t)) \\ &\approx \left(\mathsf{I}+\frac{h}{2}\Omega\right)\mathbf{f}(t)-\frac{h}{2}\Omega\mathbf{f}^{\mathrm{eq}}(t)-\frac{h}{2}\mathbf{G}(t)\end{aligned} \tag{34}$$

Using this transformation to define the auxiliary variable $\bar{\mathbf{f}}=\mathsf{C}^{-1/2}\mathbf{f}$, the collision step can be written as

$$\begin{aligned}\bar{\mathbf{f}}(t+h) &= \left(\mathsf{I}+\frac{h}{2}\Omega\right)\mathbf{f}(t+h)-\frac{h}{2}\Omega\mathbf{f}^{\mathrm{eq}}(t+h)-\frac{h}{2}\mathbf{G}(t+h) \\ &= \left(\mathsf{I}-\frac{h}{2}\Omega\right)\mathbf{f}(t)+\frac{h}{2}\Omega\mathbf{f}^{\mathrm{eq}}(t)+\frac{h}{2}\mathbf{G}(t) \\ &= \bar{\mathbf{f}}(t)-\left(1+\frac{h}{2}\Omega\right)^{-1}h\Omega\left[\bar{\mathbf{f}}(t)-\mathbf{f}^{\mathrm{eq}}(t)\right]+\left(\mathsf{I}+\frac{h}{2}\Omega\right)^{-1}h\mathbf{G}(t)\end{aligned} \tag{35}$$

and the lattice Boltzmann update is obtained in the commonly applied form

$$\begin{aligned}\bar{f}_i(\mathbf{x}+h\mathbf{c}_i,t+h)=\mathsf{SC}\bar{f}_i(\mathbf{x},t)=\bar{f}_i(\mathbf{x},t)-\sum_j\Lambda_{ij}\left[\bar{f}_j(\mathbf{x},t)-f_j^{\mathrm{eq}}(\mathbf{x},t)\right] \\ +\sum_j\left(\delta_{ij}-\frac{1}{2}\Lambda_{ij}\right)hG_j(t)\end{aligned} \tag{36}$$

Here, we have introduced the discrete collision matrix $\Lambda=\left(1+\frac{h}{2}\Omega\right)^{-1}h\Omega$. Equation [36] is the seminal *lattice Boltzmann equation* that can be shown to reproduce the Navier–Stokes equation in the incompressible limit. It is important to note that Eq. [36] describes the dynamics of the auxiliary variables $\bar{f}_i$, and the true variables have to be obtained from the transformation $f_i=\mathsf{C}^{1/2}\bar{f}_i$. This distinction is crucial for the evaluation of the hydrodynamic moments, cf. Eq. [41]. For the sake of simplicity, we will refer to the lattice Boltzmann variables as $\mathbf{f}$ from here on. A more detailed discussion of the operator splitting approach can be found in Refs. 70 and 71.

Common Lattice Boltzmann Models The lattice Boltzmann equation can be written in the succinct form

$$f_i(\mathbf{x}+h\mathbf{c}_i,t+h)=f_i^*(\mathbf{x},t)=f_i(\mathbf{x},t)+\Delta_i(\mathbf{x},t) \tag{37}$$

where f_i^* denotes post-collisional distributions, and Δ_i combines the effects of collisions and forces. Apart from the choice of the underlying lattice, the essential elements of a lattice Boltzmann model are the specification of the equilibrium distribution $\mathbf{f}^{\mathrm{eq}}$ and the collision matrix Λ. To reproduce the Navier–Stokes equation, the following conditions have to be satisfied:

- mass conservation:

$$\sum_i f_i^{\mathrm{eq}} = \rho \qquad \sum_i \Delta_i = 0 \tag{38}$$

- momentum balance:

$$\sum_i f_i^{\mathrm{eq}} \mathbf{c}_i = \rho \mathbf{u} \qquad \sum_i \Delta_i \mathbf{c}_i = h\mathbf{G} \tag{39}$$

- momentum flux:

$$\sum_i f_i^{\mathrm{eq}} \mathbf{c}_i \mathbf{c}_i = p\mathsf{I} + \rho \mathbf{u}\mathbf{u} \qquad \frac{1}{2}\sum_i \left(f_i^{\mathrm{neq}} + f_i^{\mathrm{neq}*}\right) = -\sigma \tag{40}$$

where $\sigma = \Pi - p\mathsf{I} - \rho\mathbf{u}\mathbf{u}$ is the Newtonian viscous stress. The average of pre- and post-collisional distributions $(f_i^{\mathrm{neq}} + f_i^{*\mathrm{neq}})/2$ is a consequence of the transformation [33]. Note that this also implies

$$\rho = \sum_i f_i \tag{41a}$$

$$\rho\mathbf{u} = \sum_i f_i \mathbf{c}_i + \frac{h}{2}\mathbf{G} \tag{41b}$$

$$\Pi = \frac{1}{2}\sum_i \left(f_i + f_i^*\right)\mathbf{c}_i\mathbf{c}_i \tag{41c}$$

Multi Relaxation Time Models (MRT) In general, the hydrodynamic moments are the projection of the distribution functions f_i onto Hermite polynomial tensors. If we denote the basis vectors of the Hilbert space by $\mathbf{e}_k$, the first basis vectors corresponding to density, momentum density, and momentum flux can be written as

$$e_{0i} = 1 \tag{42a}$$

$$e_{ki} = \mathsf{H}^{(1)}_{\alpha}(\mathbf{c}_i) \qquad 1 \le k \le 3 \qquad [42b]$$

$$e_{4i} = \mathsf{H}^{(2)}_{\gamma\gamma}(\mathbf{c}_i) \qquad [42c]$$

$$e_{5i} = 2\mathsf{H}^{(2)}_{xx}(\mathbf{c}_i) - \mathsf{H}^{(2)}_{yy}(\mathbf{c}_i) - \mathsf{H}^{(2)}_{zz}(\mathbf{c}_i) \qquad [42d]$$

$$e_{6i} = \mathsf{H}^{(2)}_{yy}(\mathbf{c}_i) - \mathsf{H}^{(2)}_{zz}(\mathbf{c}_i) \qquad [42e]$$

$$e_{ki} = \mathsf{H}^{(2)}_{\alpha\beta}(\mathbf{c}_i) \qquad 7 \le k \le 9 \qquad [42f]$$

These vectors satisfy the orthogonality relation

$$\sum_i w_i e_{ki} e_{li} = b_k \delta_{kl} \qquad [43]$$

A complete basis can now be constructed using the Gram–Schmidt orthogonalization procedure, and a complete set of moments (or modes) is obtained

$$m_k = \sum_i e_{ki} f_i \qquad [44]$$

The back transformation from mode space to the distributions is given by

$$f_i = w_i \sum_k b_k^{-1} e_{ki} m_k \qquad [45]$$

This transformation can also be written in matrix–vector form as

$$\mathbf{m} = \mathsf{M}\mathbf{f} \qquad \mathbf{f} = \mathsf{M}^{-1}\mathbf{m} \qquad [46]$$

where the rows of the matrix $\mathsf{M} = (e_{ki})$ are the basis vectors $\mathbf{e}_k$. The collision operator can now be transformed to mode space

$$\mathbf{f}^{\mathrm{neq}*} = (\mathsf{I} - \Lambda)\mathbf{f}^{\mathrm{neq}} = \mathsf{M}^{-1}\Gamma\mathsf{M}\mathbf{f}^{\mathrm{neq}} = \mathsf{M}^{-1}\mathbf{m}^{\mathrm{neq}*} \qquad [47]$$

where $\Gamma = \mathsf{M}(1 - \Lambda)\mathsf{M}^{-1}$ is a diagonal matrix that relaxes each moment toward its equilibrium, that is,

$$m_k^{\mathrm{neq}*} = \gamma_k m_k^{\mathrm{neq}} = (1 - \lambda_k) m_k^{\mathrm{neq}} \qquad [48]$$

Because the relaxation coefficient λ_k can be chosen separately for each symmetry group of the moments, this collision model is termed the *MRT model*. As we will see, this model subsumes most other collision models as special cases. The number of independent eigenvalues depends on the number of symmetry groups of the

underlying lattice. The D3Q19 model, for example, allows at most six independent eigenvalues.[1] Of particular relevance are the relaxation coefficients λ_s and λ_b of the traceless and the trace components of the momentum flux tensor which are related to the bulk and shear viscosities of the fluid, respectively. From the relation between the continuum collision operator and the relaxation matrix $\Omega^{-1} = h\left(\Lambda^{-1} - \frac{1}{2}\right)$ and the kinetic expressions for the viscosity, we obtain

$$\nu = hc_s^2\left(\frac{1}{\lambda_s} - \frac{1}{2}\right) \quad [49a]$$

$$\nu_b = \frac{2}{3}hc_s^2\left(\frac{1}{\lambda_b} - \frac{1}{2}\right) \quad [49b]$$

These are the well-known expressions for the shear and bulk viscosity of the LBM.[31,73] It is worth noting that the equilibrium values $\mathbf{m}^{\mathrm{eq}}$ of the moments can be freely chosen within the symmetry constraints of the lattice. Lallemand and Luo have shown that the systematic projection of the Maxwell–Boltzmann equilibrium leads to a set of equilibrium moments satisfying Galilean invariance.[32] One of the most commonly used MRT models is the D3Q19 model whose basis vectors are listed in Table 2.

Lattice Bhatnagar–Gross–Krook (LBGK) The simplest choice for the relaxation coefficients is the lattice version of the BGK model,[24] which employs a single relaxation time for all modes, that is, $\gamma_k = 1 - h\tau^{-1}$ and

$$f_i^*(\mathbf{x},t) = f_i(\mathbf{x},t) - \frac{h}{\tau}\left[f_i(\mathbf{x},t) - f_i^{\mathrm{eq}}(\mathbf{x},t)\right] \quad [50]$$

In most cases, the LBGK model is used with a second-order expansion of the equilibrium distribution

$$f_i^{\mathrm{eq}} = w_i\rho\left[1 + \frac{\mathbf{u}\cdot\mathbf{c}_i}{c_s^2} + \frac{\mathbf{uu}:\left(\mathbf{c}_i\mathbf{c}_i - c_s^2\mathbf{I}\right)}{2\,c_s^4}\right] \quad [51]$$

Due to the single relaxation time approximation, the LBGK model is limited to a fixed Prandtl number of unity $Pr = \nu/\alpha = 1$. It is also sometimes perceived to be less stable, in particular, when simulating flows at high Reynolds number Re.[68]

Two Relaxation Time Models (TRT) While the eigenvalues for the relaxation of the stress modes determine the shear and bulk viscosities of the lattice Boltzmann fluid, the remaining relaxation coefficients of the kinetic modes have no direct physical meaning on the Navier–Stokes level. While these eigenvalues are sometimes set to zero,[51,74] it has been shown that they affect the stability of the LBM and

TABLE 2 Basis Vectors of the D3Q19 Model[44]

k	e_{ki}	b_k
0	1	1
1	c_{ix}	1/3
2	c_{iy}	1/3
3	c_{iz}	1/3
4	$\mathbf{c}_i^2 - 1$	2/3
5	$3c_{ix}^2 - \mathbf{c}_i^2$	4/3
6	$c_{iy}^2 - c_{iz}^2$	4/9
7	$c_{ix}c_{iy}$	1/9
8	$c_{iy}c_{iz}$	1/9
9	$c_{iz}c_{ix}$	1/9
10	$\left(3\mathbf{c}_i^2 - 5\right)c_{ix}$	2/3
11	$\left(3\mathbf{c}_i^2 - 5\right)c_{iy}$	2/3
12	$\left(3\mathbf{c}_i^2 - 5\right)c_{iz}$	2/3
13	$\left(c_{iy}^2 - c_{iz}^2\right)c_{ix}$	2/9
14	$\left(c_{iz}^2 - c_{ix}^2\right)c_{iy}$	2/9
15	$\left(c_{ix}^2 - c_{iy}^2\right)c_{iz}$	2/9
16	$3\mathbf{c}_i^4 - 6\mathbf{c}_i^2 + 1$	2
17	$\left(2\mathbf{c}_i^2 - 3\right)\left(3c_{ix}^2 - \mathbf{c}_i^2\right)$	4/3
18	$\left(2\mathbf{c}_i^2 - 3\right)\left(c_{iy}^2 - c_{iz}^2\right)$	4/9

they can be tuned to improve the accuracy of boundary conditions at solid surfaces,[75,76] as described in the forthcoming section on boundary conditions. One can still employ a simplified MRT by using only two independent eigenvalues γ_e and γ_o for the even and odd moments, respectively. This choice is referred to as a TRT model, which can also be viewed as a simple extension of LBGK by decomposing the distributions into an even and an odd part

$$f_i^+ = \frac{1}{2}(f_i + f_{i^-}) \qquad [52a]$$

$$f_i^- = \frac{1}{2}(f_i - f_{i^-}) \qquad [52b]$$

where i^- denotes the mirror direction of i, that is, $\mathbf{c}_i = -\mathbf{c}_{i^-}$. With these definitions, the collision operator can be written in the TRT form

$$f_i^*(\mathbf{x},t) = f_i(\mathbf{x},t) - \lambda_+\left(f_i^+ - f_i^{\mathrm{eq}+}\right) - \lambda_-\left(f_i^- - f_i^{\mathrm{eq}-}\right) \qquad [53]$$

In view of Eq. [49a] for the shear viscosity, it is convenient to introduce the notation

$$\Lambda_{\pm} = \frac{1}{\lambda_{\pm}} - \frac{1}{2} \qquad \Lambda^2 = \Lambda_+ \Lambda_- \tag{54}$$

The viscosity is then given by $\nu = hc_s\Lambda_+$ and the value of Λ^2 can be tuned to improve the stability or accuracy of boundary conditions.[75,76]

Regularized Lattice Boltzmann Models The derivation of the lattice Boltzmann equation as a truncated Hermite expansion of the continuous Boltzmann equation suggests that approximation errors are mainly due to the uncontrolled dynamics of the kinetic modes. Therefore, the relaxation coefficients are often chosen such that the kinetic modes are completely projected out, that is, $\gamma_k = 0$ for $k \geq 10$. While this is straightforward to implement in any MRT model, this has also been formulated in the LBGK framework. Realizing that the kinetic modes are essentially the moments that do not fit into the Hermitian representation, a "regularized" distribution function can be written as[77–79]

$$h_i = w_i \sum_{k=0}^{N} b_k^{-1} e_{ki} m_k = f_i^{\mathrm{eq}} + w_i \sum_{k=0}^{N} b_k^{-1} e_{ki} m_k^{\mathrm{neq}} \tag{55}$$

where $N \leq m$ is the order to which the moments fit into the Hermitian representation. Note that in the basis chosen here, the projection of the kinetic moments onto the equilibrium is zero and thus $h_i^{\mathrm{eq}} = f_i^{\mathrm{eq}}$. The LBGK collision is then applied to the regularized distribution h_i

$$f_i^*(\mathbf{x},t) = h_i(\mathbf{x},t) - \frac{h}{\tau}\left[h_i(\mathbf{x},t) - f_i^{\mathrm{eq}}(\mathbf{x},t)\right] \tag{56}$$

This method is sometimes advertised as "regularized LBGK," but in fact it is yet another special case of MRT as can be seen by transforming Eq. [56] into moment space

$$f_i^* = f_i^{\mathrm{eq}} + \left(1 - \frac{h}{\tau}\right) w_i \sum_{k=0}^{N} b_k^{-1} e_{ki} \left[m_k - m_k^{\mathrm{eq}}\right] \tag{57a}$$

$$= f_i^{\mathrm{eq}} + w_i \sum_{k=0} b_k^{-1} e_{ki} \gamma_k \left[m_k - m_k^{\mathrm{eq}}\right] \tag{57b}$$

where $\gamma_k = 1 - h\tau^{-1}$ for $0 \leq k \leq N$ and $\gamma_k = 0$ for $N < k \leq m$. This recovers the MRT collision operator as in Eq. [47].

Entropic and Cascaded Lattice Boltzmann Models A main concern in developing MRT and regularized LBGK models is the stability of the LBM. At high Reynolds numbers, the non-conserved moments tend to be subject to oscillations that can cause nonlinear instabilities.[80,81] In addition to MRT models, a class of "entropic" lattice Boltzmann models has been proposed that are based on an entropy function that is maximized by locally adjusting the relaxation time.[40] In the entropic models the viscosity of the fluid varies locally, however, an alternative known as "entropic stabilizer" avoids the alterations of the viscosity by restricting the adjustments of the relaxation time to higher-order moments,[82] similar to the regularized LBGK. Another flavor of the LBM are the cascaded models that are based on "peculiar" moments.[83] The relaxation times for the peculiar moments are chosen such that Galilean invariance is recovered. Extensions of the cascaded models use factorized and cumulant schemes to define the collision process.[84,85] For details on the entropic and cascaded lattice Boltzmann models we refer the reader to the original publications.

Parameter Choice in Lattice Boltzmann Simulations As in any simulation model, a crucial step in setting up a lattice Boltzmann simulation is the choice of the parameters and their mapping to physical quantities. Most applications of the LBM make use of "lattice units" where the basic units of length is the grid spacing a and the basic unit of time is the time step h. The basic unit of mass is often only implicitly specified, but a convenient choice is $m_p = k_B T/c_s^2$ which is controlled by the temperature, cf. the section on the fluctuating lattice Boltzmann equation. Once the grid spacing and the time step have been fixed, we can write a dimensionless speed of sound $\hat{c}_s = c_s h/a$. It is important to note that in many common lattice Boltzmann models $\hat{c}_s$ is a fixed property of the underlying lattice and should not be associated with the real speed of sound which is temperature dependent. For the D2Q9 and D3Q19 models, for example, we have $\hat{c}_s = \sqrt{1/3}$. Lattice Boltzmann simulations usually operate at a lower speed of sound which is acceptable as long as the Mach number is small enough for the incompressible limit to be valid.* However, the correct viscosity of the fluid can be set by choosing the relaxation parameter for the shear/even moments (associated with $k = 5$ to $k = 9$ in Table 2)

$$\lambda_s = \frac{h}{\tau} = \lambda_+ = \left(\frac{\hat{\nu}}{\hat{c}_s^2} + \frac{1}{2} \right)^{-1} = \frac{2\,\hat{c}_s^2}{2\hat{\nu} + \hat{c}_s^2} \qquad [58]$$

where the dimensionless kinematic viscosity $\hat{\nu} = \nu h/a^2$ and $\dfrac{\hat{\nu}}{\hat{c}_s^2}$ is the inverse of the grid-scale Reynolds number, cf. Ref. 70. Linear stability requires $0 < \lambda_s < 2$ which means that the grid-scale Reynolds number must not be too large. For the further setup of a lattice Boltzmann simulation, such as setting the external force or

* This is similar to grid-based electrostatics algorithms that can operate at a lower speed of light.[86,87]

imposed flow, one has to consider the dimensionless numbers that describe the hydrodynamics of the fluid, in particular the Reynolds number *Re*, the Mach number *Ma*, and the Knudsen number *Kn*. The Reynolds number quantifies the relative importance of inertial and viscous forces. For unsteady flows, the Womersley number α is used to quantify the relative importance of transient inertial forces and viscous forces.

$$Re = \frac{uL}{\nu} \quad [59a]$$

$$\alpha = \left(\frac{\omega L^2}{\nu}\right)^{\frac{1}{2}} \quad [59b]$$

$$Ma = \frac{u}{c_s} \quad [59c]$$

$$Kn = \frac{l_{\mathrm{mfp}}}{L} \propto \frac{Ma}{Re} \quad [59d]$$

Here, L is the characteristic length scale, $l_{\mathrm{mfp}} = \frac{\nu}{c_s^2}\sqrt{\frac{\pi kT}{2m_p}} = \sqrt{\frac{\pi}{2}}\frac{\nu}{c_s}$ is the mean free path of the LB solvent, and ω is the frequency of a pulsatile flow. For a given grid resolution a, the relaxation parameter and time step can be written in terms of the dimensionless numbers as

$$\frac{1}{\lambda_s} - \frac{1}{2} = \frac{\hat{L}}{\hat{c}_s}\frac{Ma}{Re} \quad [60a]$$

$$h = \frac{\alpha^2}{\omega}\frac{Ma}{Re}\frac{\hat{c}_s}{\hat{L}} \quad [60b]$$

Mach Number Scaling Since the LBM is valid in the incompressible regime where the compressibility errors scale with the square of the Mach number, it is feasible (and often necessary) to simulate at a higher Mach number than in the real system, as long as density fluctuations remain sufficiently small. One can thus scale the Mach number in order to accelerate convergence.[88,89] With a given Reynolds number and at fixed resolution a, a scaling of the Mach number by a factor $s = Ma'/Ma$ implies a scaling of λ_s and h according to

$$s = \frac{Ma'}{Ma} = \frac{2\,\lambda_{s'}^{-1} - 1}{2\,\lambda_s^{-1} - 1} = \frac{h'}{h} \quad [61]$$

While a fixed resolution keeps the computational costs at bay, the scaling increases the grid-scale Reynolds number and will eventually push the LBM out of the stable

domain $0 < \lambda_s < 2$. On the other hand, one can keep $\hat{\nu}/\hat{c}_s^2$ fixed which implies the *diffusive scaling*

$$s = \frac{Ma'}{Ma} = \frac{a'}{a} = \frac{\sqrt{h'}}{\sqrt{h}} \qquad [62]$$

In dealing with an unstable simulation setup, it is thus often inevitable to increase the grid resolution, which can become computationally very expensive, especially if higher Reynolds numbers are desired. To address this challenge, more elaborate modifications of the LBM such as the entropic and cascaded lattice Boltzmann models mentioned earlier have been developed. It should be noted that the Knudsen number *Kn* is proportional to the ratio of the Mach number and the Reynolds number, *Ma/Re*, and therefore is also limited to a certain range of values. Essentially, the incompressible Navier–Stokes equation is recovered from the LBM in the limit $Ma/Re \to 0$ which means $Kn \to 0$.

The Fluctuating Lattice Boltzmann Equation

The LBM replaces the Boolean variables of the LGA with ensemble-averaged distributions. This eliminates the need for excessive statistical averaging and smoothes the dynamic variables. The averaged distributions are no longer subject to noise and the evolution is entirely deterministic. While this is mostly perceived as a considerable advantage over LGA methods, the lack of statistical properties limits the application of the LBM to systems where statistical fluctuations are unimportant. However, the deterministic dynamics is insufficient for modeling Brownian motion in soft matter systems. This is due to the small length and timescales in these systems, making it necessary to reintroduce some molecular level detail, that is, thermal fluctuations. This can be done systematically by augmenting the LB collision operator such that it reproduces the statistical mechanics of a generalized lattice gas model.[44,45] For an ideal gas we can determine the mass m_p of a gas particle from the equation of state $m_p c_s^2 = k_B T$. For convenience, we also introduce the parameter

$$\mu = \frac{m_p}{a^3} = \frac{k_B T}{c_s^2 a^3} \qquad [63]$$

The average number of particles on a lattice site is then given by $N_p = \rho/\mu$. In an ideal gas, the variance of N_p is equal to the mean such that the relative importance of fluctuations, the so-called *Boltzmann number Bo*, can be written as[1,45]

$$Bo = \frac{\sqrt{\left\langle N_p^2 \right\rangle - \left\langle N_p \right\rangle^2}}{\left\langle N_p \right\rangle} = \left\langle N_p \right\rangle^{-1/2} = \left(\frac{\rho}{\mu}\right)^{-1/2} = \left(\frac{k_B T}{\rho c_s^2 a^3}\right)^{1/2} \qquad [64]$$

This expression shows that thermal fluctuations become increasingly important at small lattice spacings a as they are common in soft matter applications. Moreover, for a given lattice spacing, the fluctuations can be controlled by the temperature as desired. The deterministic lattice Boltzmann equation operates at $Bo = 0$. To implement a finite Boltzmann number, we consider the number of particles associated with discrete velocity $\mathbf{c}_i$ given by the occupation number n_i:

$$n_i = \frac{f_i}{\mu} \tag{65}$$

In an ideal gas, this occupation number corresponds to the phase space occupancy and is thus Poisson distributed. The joint probability distribution of all occupation numbers on a lattice site is the product of the individual distributions subject to the constraints of conserved mass and momentum. It can be written in the Boltzmann-like form

$$P(\{n_i\}) \propto \exp[S(\{n_i\})]\delta\left(\mu\sum_i n_i - \rho\right)\delta\left(\mu\sum_i n_i\mathbf{c}_i - \mathbf{j}\right) \tag{66}$$

where we have used the associated entropy

$$S(\{n_i\}) = -\sum_i (n_i \ln n_i - n_i - n_i \ln \bar{n}_i + \bar{n}_i) \tag{67}$$

The mean values $\bar{n}_i$ can be expressed in terms of the lattice weights and the mean number of particles on the site as $\bar{n}_i = w_i N_p$. The most probable distribution can be determined by constraint maximization of the entropy S. The result $f_i^{\mathrm{eq}} = \mu n_i^{\mathrm{eq}}$ is identical to the equilibrium distribution of the deterministic model. The procedure is indeed closely related to the entropic lattice Boltzmann approaches.[38,40] Thermal fluctuations can now be introduced as deviations f_i^{neq} from the most probable distribution. Using a saddle-point approximation (see Refs. 44 and 64 for details) they are Gaussian distributed and the variance in the low-velocity approximation is given by $\mu w_i \rho$. Within the MRT model, the thermal fluctuations can be expressed in mode space by the probability distribution

$$P\left(\left\{m_k^{\mathrm{neq}}\right\}\right) \propto \exp\left[-\sum_k \frac{\left(m_k^{\mathrm{neq}}\right)^2}{2\mu b_k \rho}\right]\prod_{k\le 3}\delta\left(m_k^{\mathrm{neq}}\right) \propto \prod_{k>3}\exp\left[-\frac{\left(m_k^{\mathrm{neq}}\right)^2}{2\mu b_k \rho}\right] \tag{68}$$

This representation conveniently eliminates the constraints since the conserved moments do not fluctuate. Consequently, the fluctuations in mode space are independently Gaussian distributed with variance $\mu b_k \rho$. To implement this distribution

in the lattice Boltzmann algorithm, the collision step is reinterpreted as a Monte-Carlo process that includes a random update

$$m_k^{\mathrm{neq}*} = \gamma_k m_k^{\mathrm{neq}} + \varphi_k r_k \qquad [69]$$

where $\gamma_k = 1 - \lambda_k$ as before and r_k is a Gaussian random number with zero mean and unit variance. The update process has to satisfy detailed balance to generate the correct distribution, that is,

$$\omega\left(m_k^{\mathrm{neq}} \to m_k^{*\mathrm{neq}}\right)\exp\left[-\frac{\left(m_k^{\mathrm{neq}}\right)^2}{2\mu b_k \rho}\right] = \omega\left(m_k^{*\mathrm{neq}} \to m_k^{\mathrm{neq}}\right)\exp\left[-\frac{\left(m_k^{*\mathrm{neq}}\right)^2}{2\mu b_k \rho}\right] \qquad [70]$$

where

$$\omega\left(m_k^{\mathrm{neq}} \to m_k^{*\mathrm{neq}}\right) = \sqrt{\frac{1}{2\pi\,\varphi_k^2}}\,\exp\left[-\frac{\left(m_k^{*\mathrm{neq}} - \gamma_k\, m_k^{\mathrm{neq}}\right)^2}{2\,\varphi_k^2}\right] \qquad [71]$$

To satisfy detailed balance, we thus have to set the amplitude of the stochastic update to

$$\varphi_k^2 = \mu b_k \rho (1-\gamma_k)^2 \qquad [72]$$

It is important to note that Eq. [72] holds for *all* moments in the system. Hence, all moments except the conserved ones with $\gamma_k = 1$ are subject to fluctuations. This mitigates the deficiencies in earlier implementations of thermal fluctuations that were based on thermalization of the stress modes alone.[50,51,74] It should also be pointed out that the result of Eq. [72] is identical to the procedure proposed by Adhikari et al.[43] based on Langevin noise. The full thermalization substantially improves the thermalization at short length scales. From a general perspective, this also sheds some light on the role of the kinetic modes in the lattice model and demonstrates that, although they do not enter the macroscopic equations on the Navier–Stokes level, they do impact the dynamics of the system at higher orders. The full thermalization can thus also improve the accuracy with which transport properties of micro-suspensions are recovered, for example, the static and dynamic properties of a polymer chain in solution.[90]

Boundary Conditions

The LBM is often celebrated for the ease with which geometrically complex boundary conditions can be implemented. Nevertheless, when mapping solid objects to the discrete grid one has to carefully chose a representation that satisfies the conservation laws with sufficient accuracy. Geometric boundaries intersect the

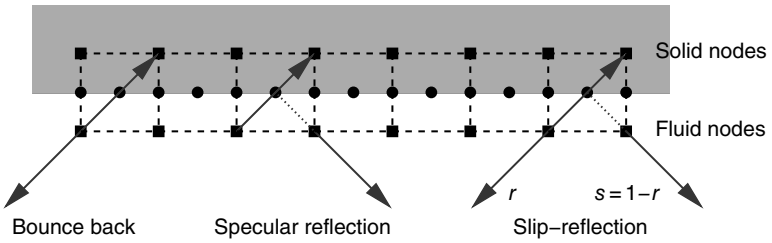

FIGURE 2 Illustration of simple midlink reflection rules. (Left) Bounce-back reverses the velocity of the impinging population. (Middle) Specular reflections reverse only the normal momentum during reflection of the populations. (Right) Slip-reflections combine bounce-back and specular reflections. *Source*: reproduced with minor modifications from Ref. 64.

links and divide the lattice into fluid nodes and solid nodes as illustrated in Figure 2. On fluid nodes that are connected to solid nodes by intersected links, one or more particle distributions are unknown after the streaming step because distributions on the solid nodes are undefined. Boundary conditions serve the purpose of finding a closure for the unknown distributions in such a way that a given macroscopic boundary condition is satisfied. In most cases, this is the no-slip (or stick) boundary condition $\mathbf{u} = 0$.

Bounce-Back The simplest and most widely used boundary condition to implement a no-slip surface in the LBM is the bounce-back rule. The unknown incoming distributions at a boundary are defined by "bouncing back" the outgoing distributions that impinge on the surface

$$f_i(\mathbf{x}, t+h) = f_{i^-}^*(\mathbf{x}, t) \qquad [73]$$

where $\mathbf{x} + h\mathbf{c}_i$ is a solid site and $\mathbf{c}_{i^-} = -\mathbf{c}_i$. For the bounce-back rule, the boundary is, to first order, located halfway between the fluid and the solid nodes. The exact location depends on the collision operator, and for the LBGK model the boundary location becomes effectively viscosity dependent. This can be mitigated by using interpolation schemes introduced below that result in a second-order accurate boundary condition for certain geometries. For moving boundaries, the bounce-back rule can be modified to incorporate the surface velocity[91]

$$f_i(\mathbf{x}, t+h) = f_{i^-}^*(\mathbf{x}, t) - \frac{2w_i \mathbf{u}_b \cdot \mathbf{c}_{i^-}}{c_s^2} \qquad [74]$$

For a moving particle, the surface velocity is obtained from

$$\mathbf{u}_b = \mathbf{U} + \omega \times (\mathbf{r}_b - \mathbf{R}) \qquad [75]$$

where **U** and ω are the velocity and angular velocity, respectively, of the particle and $\mathbf{r}_b = \mathbf{x} + \frac{1}{2}h\mathbf{c}_{i^-}$ is the midlink location. This rule guarantees that the steady-state distribution is consistent with the surface velocity. While early implementations treated the interior of the particle as fluid identical to the outside, excluding the interior nodes from the fluid leads to a more accurate description of the particle motion. Due to the motion of the particle, fluid nodes can become covered and uncovered, and the procedure to determine the corresponding distributions is described in more detail in Ref. 92. In dense suspensions, the particle separation can become very small and additional lubrication corrections are necessary to avoid depletion effects.[93,94]

Specular Reflections If a slip surface instead of a no-slip surface is desired, an equally simple boundary condition can be implemented in terms of specular reflections

$$f_i(\mathbf{x} + h[\mathbf{c}_i - \mathbf{n}(\mathbf{n}\cdot\mathbf{c}_i)], t + h) = f^*_{i^+}(\mathbf{x}, t) \qquad [76]$$

where **n** is the local surface normal and $\mathbf{c}_{i^+} = \mathbf{c}_i - 2\mathbf{n}(\mathbf{n}\cdot\mathbf{c}_i)$. This rule satisfies no mass transfer across the surface and no momentum transfer in the tangential direction. Since full slip boundary conditions are not very common in multiphase systems, specular reflections are typically combined with the bounce-back rule to produce a "partial slip" boundary condition.[64,95] The combination can be written as a slip-reflection rule[42,96,97]

$$f_i(\mathbf{x}, t) = rf_{i^-}(\mathbf{x}, t) + sf_{i^+}(\mathbf{x} - h[\mathbf{c}_i - \mathbf{n}(\mathbf{n}\cdot\mathbf{c}_i)], t) \qquad [77]$$

where the two parameters r and s have to satisfy $r + s = 1$. The slip-reflection rule leads to a surface slip velocity that is given to first order in the Knudsen number Kn:

$$u_{\text{slip}} = A\ Kn \left.\frac{\partial u_n}{\partial \hat{n}}\right|_{\mathbf{r}_b} + O\left(Kn^2\right) \qquad [78]$$

where $\mathbf{r}_b = \mathbf{x} + \frac{1}{2}h\mathbf{c}_{i^-}$ and

$$A = \frac{a}{c_s h}\frac{s}{1-s} \qquad [79]$$

An alternative way of implementing a slip boundary condition based on including surface friction force was proposed in Ref. 64, and the resulting slip velocity is identical to Eq. [78].

Interpolation Schemes As noted above, the simple bounce-back rule is only first-order accurate. The accuracy of the boundary condition can be improved by including information from sites further away from the boundary, such that a

more faithful representation of velocity gradients becomes possible. A succinct interpolation scheme that uses only distributions along one direction was proposed by Bouzidi, Firdaouss, and Lallemand (BFL). It requires knowledge of the fraction q of the intersected links that lies inside the fluid. As illustrated in Figure 3, two cases can be distinguished depending whether the intersection is located in front ($q < 1/2$) of or behind ($q \geq 1/2$) the midlink location. The BFL rule is given by

$$f_{i^-}(\mathbf{r}_b, t+h) = 2q f_i^*(\mathbf{r}_b, t) + (1-2q) f_i^*(\mathbf{r}_b - h\mathbf{c}_i, t) \qquad q < \frac{1}{2} \qquad [80a]$$

$$f_{i^-}(\mathbf{r}_b, t+h) = \frac{1}{2q} f_i^*(\mathbf{r}_b, t) + \frac{2q-1}{2q} f_{i^-}^*(\mathbf{r}_b, t) \qquad q \geq \frac{1}{2} \qquad [80b]$$

For $q = 1/2$, this reduces to the standard bounce-back rule. To make the boundary condition second-order accurate, the BFL rule has to be used with an MRT collision model that sets the relaxation coefficients for the kinetic moments such that the location of the boundary is independent of the fluid viscosity. The simplest choice is a TRT model with

$$\lambda_-(\lambda_+) = \frac{8(2-\lambda)}{8-\lambda} \qquad [81]$$

which corresponds to $\Lambda^2 = 3/16$. In dense suspensions, there may not be sufficient fluid sites between particle surfaces to apply the BFL rule. For this situation, one can resort to a modification of the BFL rule that interpolates only the equilibrium distribution f_i^{eq} and resorts to simple bounce-back for the nonequilibrium distributions

$$f_{i^-}^{\mathrm{eq}}(\mathbf{r}_b, t+h) = 2q f_i^{\mathrm{eq}}(\mathbf{r}_b, t) + (1-2q) f_i^{\mathrm{eq}}(\mathbf{r}_b - h\mathbf{c}_i, t) \qquad q < \frac{1}{2} \qquad [82a]$$

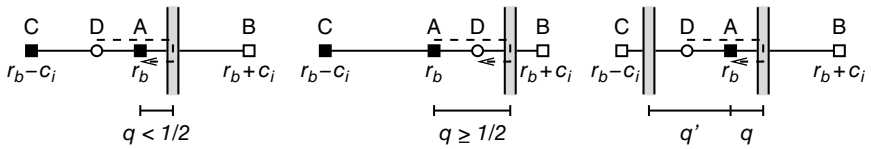

FIGURE 3 Illustration of the interpolation rules used in the boundary condition by Bouzidi et al.[98] The boundary intersects the link between fluid site A and solid site B such that a fraction q of the link lies within the fluid. Depending on the value of q, either a pre-collision (left, with D interpolated from A and C) or a post-collision (right, A is interpolated from C and D) interpolation is applied to determine the unknown distribution at A, cf. Eq. [80]. The rightmost picture shows the case where only one lattice node is present between two surfaces. While the BFL scheme is not applicable any more, equilibrium interpolation is still possible. *Source*: reproduced from Ref. 64.

$$f_{i^-}^{\mathrm{eq}}(\mathbf{r}_b, t+h) = \frac{1-q}{q} f_i^{\mathrm{eq}}(\mathbf{r}_b, t) + \frac{2q-1}{q} f_i^{\mathrm{eq}}(\mathbf{r}_b + qh\mathbf{c}_i) \qquad q \geq \frac{1}{2} \tag{82b}$$

$$f_{i^-}^{\mathrm{neq}}(\mathbf{r}_b, t+h) = f_i^{\mathrm{neq}}(\mathbf{r}_b, t) \tag{82c}$$

where $f_i^{\mathrm{eq}}(\mathbf{r}_b + qh\mathbf{c}_i)$ is the boundary equilibrium. This boundary condition is still second-order accurate, since the nonequilibrium part f_i^{neq} enters the dynamics an order higher than the equilibrium part. If only one fluid site is available between the surfaces, the equilibrium distribution is interpolated from the value at the two surfaces according to

$$f_{i^-}^{\mathrm{eq}}(\mathbf{r}_b, t+h) = \frac{q' + 2q - 1}{q'} f_i^{\mathrm{eq}}(\mathbf{r}_b, t) + \frac{1-2q}{q'} f_i^{\mathrm{eq}}(\mathbf{r}_b - q'h\mathbf{c}_i) \tag{83}$$

where q' is the fraction of the link $\mathbf{c}_{i^-}$ outside the second surface, cf. Figure 3. For flat surfaces that are not aligned with the lattice directions, the value of the relaxation eigenvalue λ_- can be further tuned. It was shown numerically that the equilibrium interpolation yields more accurate results than the linear and quadratic interpolation rules.[76] It should be noted, however, that the interpolation rules are not strictly mass conserving, and the possible mass leakage should be monitored carefully and corrected as necessary.[99]

On-Site Closure Schemes Instead of determining the distributions at a boundary site from the available distributions on the nearby fluid nodes, it is also possible to determine the distributions from the desired values of the hydrodynamic moments *on* a site. We refer to these boundary conditions as *on-site closure schemes*. They essentially require an inverse mapping of the moments to the distributions where certain distributions are already known.[100–103] The most common application for on-site boundary conditions is the imposition of a Dirichlet condition for the flow velocity u_b. For a plane surface with normal $\mathbf{n}$ pointing into the fluid, the distributions can be separated in unknown ($\mathbf{n}\cdot\mathbf{c}_i > 0$), impinging ($\mathbf{n}\cdot\mathbf{c}_i < 0$), and grazing ($\mathbf{n}\cdot\mathbf{c}_i = 0$) distributions according to the sign of $\mathbf{n}\cdot\mathbf{c}_i$. The mass and momentum densities on a boundary node can thus be written as

$$\rho = \sum_i f_i = \sum_{c_{in}<0} f_i + \sum_{c_{in}=0} f_i + \sum_{c_{in}>0} f_i \tag{84a}$$

$$\rho u_b = \sum_i f_i c_{in} = \sum_{c_{in}<0} f_i c_{in} + \sum_{c_{in}>0} f_i c_{in} = -\sum_{c_{in}<0} f_i + \sum_{c_{in}>0} f_i \tag{84b}$$

where $c_{in} = \mathbf{n}\cdot\mathbf{c}_i$ and the last equality is valid for lattices where $|c_{in}| = 1$ which includes, *inter alia*, D2Q9 and D3Q19. The unknown distributions can be eliminated and the density can be expressed in terms of known distributions as

$$\rho = \frac{1}{1-u_{B,z}}\left(2\sum_{c_{iz}<0} f_i + \sum_{c_{iz}=0} f_i\right) \quad [85]$$

To determine the unknown distributions, one applies the bounce-back rule to the nonequilibrium part and obtains

$$f_i = f_i^{\mathrm{eq}} + \left(f_{i^-} - f_{i^-}^{\mathrm{eq}}\right) = f_{i^-} + w_i\rho\frac{\mathbf{u}_b\cdot\mathbf{c}_i}{c_s^2} - w_i\rho\frac{\mathbf{u}_b\cdot\mathbf{c}_{i^-}}{c_s^2} + O\left(u_b^3\right) \quad [86]$$

The resulting equation system is typically underdetermined, and additional conditions have to be introduced. A practical assumption is to specify the momentum flux induced by the boundary conditions, which leads to a closure for the nonequilibrium distributions

$$\frac{\rho h\, c_s^2}{\lambda}\left(\frac{\partial u_\alpha}{\partial r_\beta} + \frac{\partial u_\beta}{\partial r_\alpha}\right) = \sum_{c_{in}>0} f_i^{\mathrm{neq}} c_{i\alpha}c_{i\beta} + \sum_{c_{in}=0} f_i^{\mathrm{neq}} c_{i\alpha}c_{i\beta} + \sum_{c_{in}<0} f_i^{\mathrm{neq}} c_{i\alpha}c_{i\beta} \quad [87]$$

The detailed calculation for the D3Q19 model and generalization to arbitrary flow directions can be found in Ref. 103. A more comprehensive overview of the various available boundary conditions for the LBM is available in Ref. 64.

The use of boundary conditions for lattice Boltzmann simulations of suspended particles has been pioneered by Ladd.[49–51,91,104,] Starting from the simple bounce-back boundary condition, these simulations have driven a number of algorithmic improvements that increased the accuracy of the results for diffusion and sedimentation.[74,92,105] Improved boundary schemes and lubrication corrections have further enabled simulations of dense suspensions with particles that are almost in contact with each other.[76,93,94,105] Colloidal suspensions have also been investigated in shear flow simulations, and the dependence of the transport properties on the structure has been investigated along with formation and growth of clusters.[106–109] More recently, rigid particles have also been studied in multiphase fluids where the particles can assemble at the interface and prevent phase separation, leading to materials such as particle-stabilized emulsions and bijels.[110] Another example are nanoparticles on a droplet in shear flow as depicted in Figure 4.[111] The behavior of anisotropic particles at interfaces and their interactions with external fields are interesting applications that are increasingly being explored by simulations.[112–114]

Fluid–Particle Coupling

In soft matter systems, suspended objects often have internal degrees of freedom that are governed by molecular-level interactions. For such systems, a true multiscale approach is needed to capture the complex dynamics that may involve

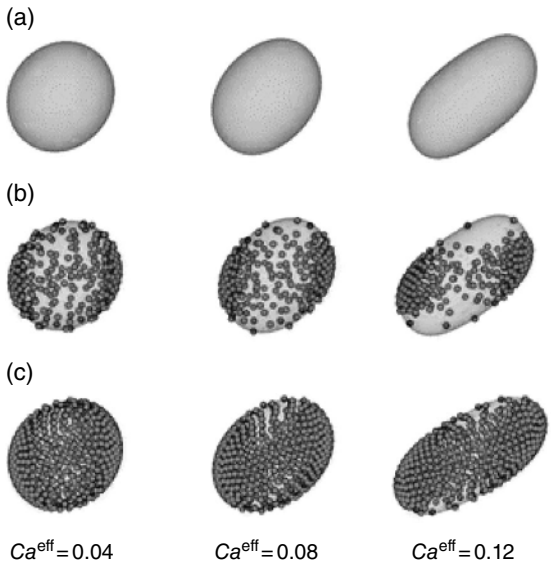

FIGURE 4 Nanoparticles on a droplet in shear flow at different particle coverage fractions χ and effective capillary number Ca^{eff}. The particle coverage fractions are (a) $\chi = 0.0$, (b) $\chi = 0.27$, and (c) $\chi = 0.55$, respectively. The droplet was simulated using a Shan–Chen multiphase model and the nanoparticles were treated with the moving bounce-back boundary condition [74]. *Source*: from Ref. 111 with permission from The Royal Society of Chemistry. (See color plate section for the color representation of this figure.)

changes to the shape of the object. A very successful method that was first developed for polymer chains is based on *force coupling*.[52,53,71,115] The suspended particles are considered point-like and their positions $\mathbf{r}_i(t)$ and velocities $\mathbf{v}_i(t)$ are updated according to Newton's equation of motion using molecular dynamics (MD)

$$\frac{d}{dt}\mathbf{r}_i(t) = \mathcal{P}\mathbf{r}_i(t) = \mathbf{v}_i(t) \tag{88a}$$

$$\frac{d}{dt}\mathbf{v}_i(t) = \mathcal{F}\mathbf{v}_i(t) = \frac{1}{m_i}\left(\mathbf{F}_i^h + \mathbf{F}_i^{\text{int}}\right) \tag{88b}$$

where $\mathbf{F}_i^{\text{int}}$ are the internal (conservative) interaction forces, and $\mathbf{F}_i^h$ is a hydrodynamic coupling force.

Force Coupling The basic idea for the fluid–particle coupling is that the particles experience a Stokes-like drag force when moving with a relative velocity with respect to the flow[53]

$$\mathbf{F}_i^h(t) \;\; = -\Gamma_i[\mathbf{v}_i(t) - \mathbf{u}(\mathbf{r}_i, t)] + \boldsymbol{\zeta}_i \qquad [89]$$

where Γ_i is a friction constant, and $\boldsymbol{\zeta}_i$ is a stochastic force required to satisfy detailed balance. The fluid velocity $\mathbf{u}(\mathbf{r}_i, t)$ at the particle's position (see Figure 5) is determined by an interpolation procedure

$$\mathbf{u}(\mathbf{r}_i, t) = \mathcal{I}_a[\mathbf{r}_i(t)]\mathbf{u}(\mathbf{x}, t) \qquad [90]$$

where $\mathcal{I}_a[\mathbf{r}_i(t)]$ is an interpolation operator that depends on the Lagrangian positions $\mathbf{r}_i$. The interpolation scheme is illustrated in Figure 5. To obey momentum conservation, the negative of the friction force has to be applied to the fluid as a reaction force

$$\mathbf{F}^h(\mathbf{x}, t) = -\mathcal{I}_a^*[\mathbf{r}_i(t)]\mathbf{F}_i^h(t) \qquad [91]$$

where $\mathcal{I}_a^*$ is the adjoint operator of $\mathcal{I}_a$. In principle, the force in Eq. [89] can be easily integrated in a velocity-Verlet algorithm, and the reaction force can be included as an external force in the lattice Boltzmann algorithm. However, the drag force $\mathbf{F}^h$ depends on the particle velocity, the fluid velocity, and the entire configuration through the interpolation operator $\mathcal{I}_a$, such that the update equations for the velocities become implicit. Another concern involves the role of the intrinsic forces $\mathbf{F}_i^{\text{int}}$. Consistent with standard MD algorithms that integrate Newton's equation of motion as in Eq. [88] the intrinsic forces are typically applied only to the particle system. However, in a coarse-grained description, it might not always be suitable to keep this separation and the intrinsic forces could also act on the fluid (an extreme

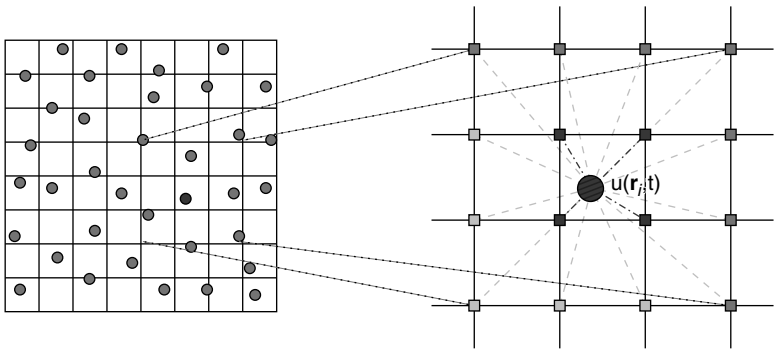

FIGURE 5 Two-dimensional illustration of the interpolation operator $\mathcal{I}[\mathbf{r}_i]$. The velocity $\mathbf{u}(\mathbf{r}_i, t)$ at the particle's position $\mathbf{r}_i$ is determined from the surrounding lattice sites. For linear interpolation, the four nearest neighbors are used. Three-point interpolation uses an additional point per direction, while four-point interpolation uses the entire second neighbor shell.

case is the immersed boundary method (IBM) where the intrinsic forces act entirely on the fluid). To address this ambiguity, we introduce a parameter $\mathfrak{r}$ that controls the fraction of the force that is applied to the particle and to the fluid system. The velocity equations can then be written in the generalized form[71]

$$\frac{\partial}{\partial t}\mathbf{v}_i(t) = -\frac{1}{m_i}\left[\Gamma_i(\mathbf{v}_i - \mathbf{u}(\mathbf{r}_i,t)) - \boldsymbol{\zeta}_i - (1-\mathfrak{r})\mathbf{F}_i^{\text{int}}\right] \tag{92a}$$

$$\frac{\partial}{\partial t}\mathbf{u}(\mathbf{r}_i,t) = \frac{1}{\rho a^3}\left[\Gamma_i(\mathbf{v}_i - \mathbf{u}(\mathbf{r}_i,t)) - \boldsymbol{\zeta}_i + \mathfrak{r}\mathbf{F}_i^{\text{int}}\right] \tag{92b}$$

Note that in most implementations $\mathfrak{r} = 0$ is chosen. Assuming that only one particle affects the fluid velocity on the surrounding lattice sites (the general case involves a matrix system but can in principle be treated in the same way), these equations can be solved using the Crank–Nicolson rule to obtain the discrete velocity updates

$$\mathbf{v}_i(t+h) = \mathbf{v}_i(t) - \frac{\Gamma_i^{-1}\alpha}{1+\frac{\alpha}{2}+\frac{\beta}{2}}\left[\Gamma_i(\mathbf{v}_i(t) - \mathbf{u}(\mathbf{r}_i,t)) - \boldsymbol{\zeta}_i - \left(1+\frac{\beta}{2}-\mathfrak{r}\right)\mathbf{F}_i^{\text{int}}\right] \tag{93a}$$

$$\mathbf{u}(\mathbf{r}_i,t+h) = \mathbf{u}_i(\mathbf{r}_i,t) + \frac{\Gamma_i^{-1}\beta}{1+\frac{\alpha}{2}+\frac{\beta}{2}}\left[\Gamma_i(\mathbf{v}_i(t) - \mathbf{u}(\mathbf{r}_i,t)) - \boldsymbol{\zeta}_i + \left(\frac{\alpha}{2}+\mathfrak{r}\right)\mathbf{F}_i^{\text{int}}\right] \tag{93b}$$

where we have introduced the parameters $\alpha = \frac{h\Gamma_i}{m_i}$ and $\beta = \frac{h\Gamma_i}{\rho a^3}$. Comparison with a midpoint scheme leads to the midpoint coupling force

$$\mathbf{F}_i^h\left(t+\frac{h}{2}\right) = -\frac{1}{1+\frac{\alpha}{2}+\frac{\beta}{2}}\left[\Gamma_i(\mathbf{v}_i(t) - \mathbf{u}(\mathbf{r}_i,t)) - \boldsymbol{\zeta}_i + \left(\frac{\alpha}{2}(1-\mathfrak{r}) - \frac{\beta}{2}\mathfrak{r}\right)\mathbf{F}_i^{\text{int}}\right] \tag{94}$$

This is a slightly modified version of the algorithm presented in Refs. 1 and 116, where $\mathfrak{r} = 0$ was used and where a constant flow velocity $\mathbf{u}(\mathbf{r}, t)$ was assumed during each time step. The stochastic force $\boldsymbol{\zeta}_i$ has to be determined such that the system obeys detailed balance. The detailed calculations involve a Kramers–Moyal expansion, which is explained in detail in Ref. 1.

An important property of the viscous force coupling is that the bare friction parameter Γ_i is not the effective physical friction. The latter is subject to a renormalization that can be determined by considering a single particle that is dragged with a constant force. Since the reaction force of the drag is applied to the fluid, we can determine the fluid velocity at the particle's center[1]

$$\mathbf{u} = \frac{1}{g\eta a}\mathbf{F} = \frac{\Gamma_i}{g\eta a}(\mathbf{v}-\mathbf{u}) = \frac{\Gamma_i}{g\eta a}\left(\mathbf{v} - \frac{1}{g\eta a}\mathbf{F}\right) \tag{95}$$

The factor $(g\eta a)^{-1}$ is a result of translational invariance and dimensional considerations, and g is left as a calibration factor. The particle velocity can then be written as

$$\mathbf{v} = \left(\frac{1}{\Gamma_i} + \frac{1}{g\eta a}\right)\mathbf{F} = \frac{1}{\Gamma_{\text{eff}}} \qquad [96]$$

which shows that the effective friction is given by

$$\frac{1}{\Gamma_{\text{eff}}} = \frac{1}{\Gamma_i} + \frac{1}{ga} \qquad [97]$$

where the term $(ga)^{-1}$ accounts for the renormalization. The numerical factor g depends on the details of the interpolation procedure but is independent of system size and fluid viscosity. For a given interpolation operator $\mathcal{I}[\mathbf{r}_i]$, the effective friction may change with the location of the particle on the underlying lattice Boltzmann grid. Ladd carried out a systematic analysis of the settling velocity of a single particle in a periodic cell as a function of position.[1] It was found that the factor g varies with grid position by up to 20% for a linear interpolation scheme, by about 3% for a three-point scheme, and by <1% for four-point interpolation. Since the three-point scheme requires only 27 grid points (compared to 64 for four-point interpolation) and establishes a more localized boundary surface, it is the recommended choice in LB simulations.

The force coupling algorithm was first introduced by Ahlrichs and Dünweg to simulate polymer chains in a solvent.[52–54] In these simulations, the input friction was calibrated to reproduce the same monomer diffusion as in MD simulations, resulting in a value of $\Gamma_i = 20.8$.[53] The early results for static and dynamic properties of polymer chains were obtained with a version of the lattice Boltzmann algorithm that only thermalized the stress moments. The results were replicated by Pham et al.[90] using a fully consistent thermalization procedure and carefully validated against Brownian dynamics simulations. In similar simulations, Ladd et al.[116] have established that the results of lattice Boltzmann and Brownian dynamics agree within 1%–2%. In confined geometries, the particle-fluid coupling has been used to study polymer translocation through a pore,[117] and migration of polymers and polyelectrolytes.[118–120] If the coupled particles are charged, one can combine the force coupling with electrostatics algorithms to simulate electroosmotic flow and electrophoretic phenomena,[121–123] including nanopore translocation of charged macromolecules.[124,125] Recently, the force coupling was combined with a Shan–Chen multiphase approach to study bicontinuous phase formation in polyelectrolyte solutions.[126] Figure 6 shows the effect of a colloid moving across the interface of a binary fluid. This method also adds the possibility to incorporate local solvation effects into the particle fluid coupling which paves the way to a variety of novel applications of multiphase lattice Boltzmann models.

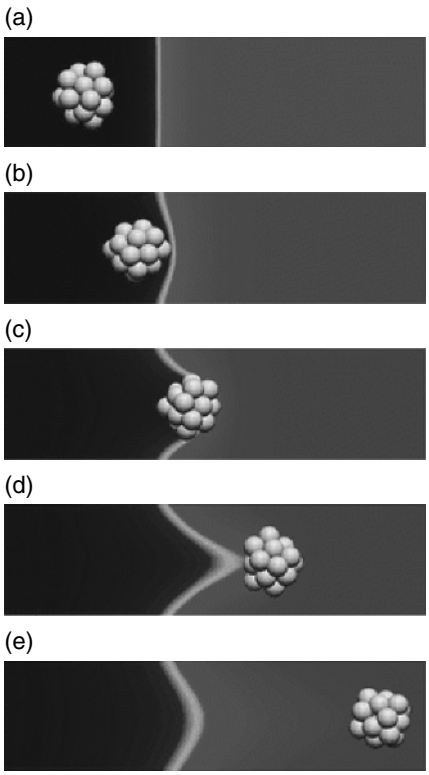

FIGURE 6 A colloid moving across the interface of a binary fluid. The colloid was simulated using the raspberry model, and a constant force was applied to push it through the interface. *Source*: reproduced from Ref. 126 with permission from The Royal Society of Chemistry.

While initially developed for suspended molecules with internal degrees of freedom, the force coupling has also been used for rigid colloidal particles.[127–129] The model is based on constructing a spherical object of particles that are connected by springs and form a surface mesh. Due to the bead-like particles the surface has a corrugated appearance, cf. Figure 6, which has led to the name "raspberry model." The model has been used to study the electrophoretic properties of charged colloids.[130,131] The raspberry model has recently been revisited and the accuracy was critically examined. It was found that filling the hollow raspberry model with additional coupling points can substantially improve the accuracy of the translational and rotational mobility. In addition, non-convex shapes were considered, and in a second study the raspberry model was investigated in confinement.[132,133]

Whereas rigid colloidal particles have been modeled using LBMs for several decades, the force coupling has more recently opened up the possibility to simulate deformable objects. Perhaps the most prominent examples are suspensions of red

blood cells that can be modeled as a deformable elastic membrane embedded in a lattice Boltzmann fluid. For example, Aidun and coworkers have used a particular version of the force coupling with an external boundary force (EBF).[134–137] An alternative approach is to use an immersed boundary model,[138] which can be translated from a finite-element version to the LBM.[139,140] As we will see below, the immersed boundary formulation is indeed a special case of the generalized force coupling method described above.

In the above studies, the coefficient r introduced in Eq. [92] was typically set to zero. We can shed some light on the role of this coefficient by calculating the deviation from a no-slip boundary condition. The difference between the particle and the fluid velocity is given by

$$\begin{aligned}\mathbf{v}_i(t+h)-\mathbf{u}(\mathbf{r}_i,t+h) &= \frac{1-\frac{\alpha}{2}-\frac{\beta}{2}}{1+\frac{\alpha}{2}+\frac{\beta}{2}}(\mathbf{v}_i(t)-\mathbf{u}(\mathbf{r}_i,t)) \\ &+ \frac{\alpha+\beta}{1+\frac{\alpha}{2}+\frac{\beta}{2}}\frac{\boldsymbol{\zeta}_i}{\Gamma_i}+\frac{\alpha(1-\mathfrak{r})-\beta\mathfrak{r}}{1+\frac{\alpha}{2}+\frac{\beta}{2}}\frac{\mathbf{F}_i^{\text{int}}}{\Gamma_i}\end{aligned} \quad [98]$$

The second term is a thermal fluctuation that is zero on average. To eliminate the last term, we require $\alpha(1-\mathfrak{r})-\beta\mathfrak{r}=0$ which implies

$$\mathfrak{r}=\frac{\alpha}{\alpha+\beta}=\frac{1}{1+\frac{m_i}{\rho a^3}} \quad [99]$$

This suggests that the distribution of the intrinsic force between the particle and the fluid is controlled by the ratio of the particle mass m_i and the fluid mass of one lattice cell ρa^3. The limiting cases are actually well-known coupling algorithms: in the limit $m_i \gg \rho a^3$ we have $\mathfrak{r}\to 0$, and the intrinsic force is only applied to the particle system. This method is known as external boundary force (EBF) where $\Gamma_i=\frac{\rho a^3}{h}$ or $\beta=1$. The EBF "forces" the fluid to move at the surface velocity.[136,141] Conversely, in the limit $m \ll \rho a^3$ we have $\mathfrak{r}\to 1$ and the intrinsic force is entirely applied to the fluid. In this case, the particles are simply advected with the fluid which is known as the immersed boundary method (IBM). The coefficient $\mathfrak{r}$ thus describes how immersed the particles are within the fluid, and it is hence referred to as the *immersion number*.[71] Since $\mathfrak{r}$ is independent of Γ_i, it can be used to tune the transfer of intrinsic forces between the particles and the fluid. It should be noted that the immersion number also depends on resolution and approaches zero in the continuum limit $a\to 1$ as the mass of a lattice site becomes infinitely small. A systematic numerical analysis of these limits is left for future work and the practical impact of the parameter $\mathfrak{r}$ is an open research question.

LBM FOR MULTIPHASE FLUIDS

We will begin with the set of continuum equations that capture the dynamics of the binary fluid (or two fluid phases interacting based on a chosen interaction potential). Then, we will give a few examples where these equations are numerically integrated using the free-energy multiphase LBM in both two and three dimensions. We will then focus on the implementation of the multiphase LBM and conclude this section with some remarks on a well-known issue in multiphase LBM, known as "spurious velocities," and possible strategies to minimize these spurious velocities.

Governing Continuum Equations

To describe the dynamics of the binary fluid using the free-energy lattice Boltzmann approach, we first define an order parameter, which is the difference between the densities of the phases A and B and can be written as $\varphi(\mathbf{x}) = \rho^{A}(\mathbf{x}) - \rho^{B}(\mathbf{x})$,[5,142] where $\rho^{A}(\mathbf{x})$ and $\rho^{B}(\mathbf{x})$ are the densities of each of the components. Correspondingly, the total density of the system is defined as $\rho(\mathbf{x}) = \rho^{A}(\mathbf{x}) + \rho^{B}(\mathbf{x})$. The interface between the phases varies smoothly across a number of lattice sites such that in equilibrium the order parameter changes gradually across the interface, typically from the value set to "−1" within the A phase to "+1" within the B as we show below (with the total dimensionless density set to unity). It is worth noting that the width of the interface between the fluid phases in LBM, as well as in many other diffuse interface models, typically exceeds significantly the interface width in real experimental systems when one relates the dimensionless values used in simulations and corresponding experimental values. Therefore, the relationship between length scales and timescales should be made carefully based on the interfacial tension of the system (see the end of this section).

First, we specify the full set of continuum equations that are effectively integrated numerically using a multiphase LBM approach with respective continuum boundary conditions. One should keep in mind that various computational fluid dynamics (CFD) techniques can be used to solve this system of continuum equations. However, a major advantage of multiphase LBM is the relative ease of implementation, including cases of complex boundary conditions encompassing chemically and topographically patterned walls, as well as computational efficiency of simulations and straightforward parallelization of the code.

Defining Total Free Energy The starting point of the LBM free-energy approach is defining a suitable free-energy potential. The specific form of this potential depends on the system of interest. One of the most common choices is the Landau free-energy potential:

$$F = \int dV \left[\Psi(\phi, \rho, T) + \frac{\kappa}{2} |\nabla \phi|^2 \right] + \int dS \Psi_s(\phi_s) \qquad [100]$$

Defining Bulk Free Energy The first term, $\Psi(\phi, \rho, T)$, represents the bulk free energy and depends on the local density, ρ, order parameter, φ, and a temperature of system, T, at a given moment in time. The first integral in Eq. [100] is taken over the entire volume of the fluid. The particular choice of this functional depends on the system of interest. This functional is often taken as[143,144]

$$\Psi(\phi,\rho,T) = \frac{c^2}{3}\rho \ln\rho - \frac{a}{2}\phi^2 + \frac{b}{4}\phi^4 \qquad [101]$$

where $c = \Delta x/\Delta t$ and $\frac{c^2}{3}$ is a dimensionless temperature.[143,145] Note that in this section we use the notation Δx for the grid spacing a, and Δt for the time step h. In general, the coefficient a in the above equation depends on the temperature within the system.[142] If the temperature is below the corresponding critical temperature, the fluids are immiscible and undergo phase-separation when quenched from the homogeneous mixture. In this case, the coefficients in Eq. [101] are chosen to be positive and the potential above represents a so-called double-well potential.[142] Typically, the depth of the minima corresponding to the pure A and pure B phases are chosen to be equal. Moreover, one often chooses $b = a$, so that the equilibrium values of the order parameter are set at "−1" and "+1" for the A and B phases, respectively, as mentioned above. We note that one could increase the temperature above the critical value, which would result in a change in sign of the parameter a, and instead of the double-well potential, the free energy will only have a single minimum corresponding to the uniformly intermixed phase. The first term in Eq. [101] depends on the total density of the fluid and is chosen in this functional form to improve numerical accuracy.

Additional interactions can be added to this system in a straightforward manner. For example, if nanoparticles with preferential wetting interactions are dispersed within the system, a corresponding potential energy favoring one of the phases[146–151] could be added as an additional term in Eq. [100]. Another form of the free-energy potential often used in the free-energy multiphase LBM[5,152] explicitly includes the repulsive energy term between the two components, $\lambda\rho^A\rho^B$, where λ is the strength of repulsion, reads:

$$\psi(\phi,\rho,T) = \frac{\lambda\rho}{4}\left(1 - \frac{\phi^2}{\rho^2}\right) - T\rho + \frac{T}{2}(\rho+\phi)\ln\left(\frac{\rho+\phi}{2}\right) + \frac{T}{2}(\rho-\phi)\ln\left(\frac{\rho-\phi}{2}\right) \qquad [102]$$

Here again the free-energy potential takes a double-well potential form similar to that in [101], but the enthalpic and entropic contributions are accounted for explicitly. In this review, we will restrict ourselves to the bulk free-energy potential given by Eq. [101].

Defining Gradient Term and Interactions with Surface The second term in Eq. [100], Ψ_s, describes the cost of forming the interface between the two phases; the interfacial tension between the two phases is proportional to the $\sqrt{\kappa}$ as we

derive below. Finally, the last term in Eq. [100] accounts for the interaction between the fluids and bounding surfaces. It is through this term that one can account for the specific wetting interactions between the binary fluid and the surrounding substrates. This surface energy could be written as a power series in ϕ_s, where ϕ_s is the value of the order parameter on the surface;[153,154] however, it is typically sufficient to take into account only a linear term:[144,151]

$$\Psi_s(\phi_s) = -h\phi_s \qquad [103]$$

Macroscopic Evolution Equations Under isothermal conditions, the dynamics of the binary fluid can be described by the system of equations encompassing the continuity equation, the advection–diffusion equation for the order parameter and the Navier–Stokes equation. This system of equation ensures conservation of total density, order parameter, and the fluid momentum, respectively, and can be written as

$$\partial_t \rho + \nabla\cdot(\rho\mathbf{u}) = 0 \qquad [104a]$$

$$\partial_t \phi + \nabla\cdot(\phi\mathbf{u}) = M\nabla^2\mu \qquad [104b]$$

$$\partial_t(\rho\mathbf{u}) + \nabla\cdot(\rho\mathbf{u}\mathbf{u}) = -\nabla\cdot\mathbf{P} + \eta\nabla^2\mathbf{u} \qquad [104c]$$

where u is the fluid velocity, η is the viscosity, and M is the mobility of the order parameter. The chemical potential μ and pressure tensor P are determined based on the chosen expression for the free energy. Taking the functional derivative of the free energy given in Eq. [100], one derives both the chemical potential and the boundary conditions on the bounding surfaces of the simulation box. For the bulk free-energy expression given in Eq. [101], the chemical potential is written as[5,144]

$$\mu = \frac{\delta F}{\delta \phi} = -a\phi + b\phi^3 - k\partial_\alpha\partial_\alpha\phi \qquad [105]$$

Finally, the pressure tensor for the same free energy reads[5,143,145,152]

$$P_{\alpha\beta} = p_0\delta_{\alpha\beta} + k\left(\partial_\alpha\phi\partial_\beta\phi - 1/2\partial_\gamma\phi\partial_\gamma\phi\delta_{\alpha\beta} - \phi\partial_\gamma\partial_\gamma\phi\delta_{\alpha\beta}\right) \qquad [106]$$

where

$$p_0 = -\Psi(\phi,\rho) + \rho\frac{\partial\Psi(\phi,\rho)}{\partial\rho} + \phi\frac{\partial\Psi(\phi,\rho)}{\partial\phi} = \frac{c^2\rho}{3} - \frac{a}{2}\phi^2 + \frac{3b}{4}\phi^4 \qquad [107]$$

Notably, while the LBM studies focusing on the hydrodynamics of phase separation are relatively recent, the same evolution equation as in Eq. [104b] (also

referred to as a Cahn–Hilliard equation, with the chemical potential defined as given in Eq. [105]) has been used to model dynamics of phase separation with conserved order parameter in a number of earlier studies in the absence of the hydrodynamic effects.[155–157]

Defining Boundary Conditions The above system of equations needs to be supplemented by boundary conditions, formulated based on the problem at hand. Multiphase LBM is successfully used to model a class of problems that focus on bulk phase separation of initially uniform mixtures quenched into the region where these mixtures undergo phase-separation. In this case, periodic boundary conditions are used and it is important to identify any possible finite size effects on the simulation results. For example, a domain growth exponent calculated from the simulations should not depend on the size of the simulation box. In many cases of interest, the binary fluid is bounded by the surrounding surfaces in one or more dimensions. Figures 8 and 9 give two examples of the multiphase free-energy LBM approach to solve problems involving interactions between droplets and structured surfaces—we will focus on these examples further below. In both of these examples, the specific contact angle was set at the structured surfaces.

We remind the reader that the contact angle θ is the angle that a liquid/vapor interface, or the interface between the two fluids, forms with the solid surface; the case of $\theta = 0$ corresponds to complete wetting, whereas the case of $0 < \theta = 0 < \pi$ corresponds to partial wetting. We now show how one can set a desired contact angle within the free-energy LBM formalism. To specify the contact angle on the surface, we need to use the last term in Eq. [100] to set the boundary conditions for the order parameter on the bounding surfaces. If the surface potential is taken in the form given in Eq. [103], the boundary condition for the order parameter can be written as

$$\mathbf{n}\cdot\nabla\phi = -\frac{h}{\kappa} \qquad [108]$$

where $\mathbf{n}$ is the unit vector normal to the boundary surface. The parameter h is a model parameter that allows one to set the static contact angle, θ, at the surface using the following relationship:[144,158]

$$h = \sqrt{2kb}\,\mathrm{sgn}\left(\frac{\pi}{2}-\theta\right)\left[\cos\left(\frac{\alpha}{3}\right)\left(1-\cos\left(\frac{\alpha}{3}\right)\right]^{1/2}\right. \qquad [109]$$

where $\alpha = \arccos\left(\sin^2\theta\right)$ and sgn(y) gives the sign of y. The details of derivation for this equation, as well as its implementation for the case of liquid–vapor interface in contact with the solid surface, are given in Refs. 158 and 159. In essence, by setting the value of h, one can define the boundary conditions that accurately reproduce Young's equation in equilibrium:

$$\cos(\theta) = \frac{\sigma_{s\mathrm{A}} - \sigma_{s\mathrm{B}}}{\sigma} \qquad [110]$$

where the values of $\sigma_{s\mathrm{A}}$ and $\sigma_{s\mathrm{B}}$ define the surface tension between the substrate and fluid A and fluid B, respectively, and σ defines the interfacial tension between the phases A and B. It is useful to keep in mind that the accuracy of setting the static contact angle through Eq. [109] and implementing this boundary condition is within 3 % for the large range of values of $30^\circ < \theta < 150^\circ$.[158]

For the velocity field, one often chooses no-slip boundary conditions (zero velocity at the walls). As we noted above, the multiphase free-energy LBM is formulated for both liquid–gas and binary fluid systems. For the binary fluid, the density of fluid remains close to the constant value (typically chosen to be unity). For liquid–gas binary systems, one would need to impose the respective densities at the bounding surfaces.

Minimization of the free energy with respect to the variations in ϕ gives that in equilibrium the chemical potential μ is equal to zero.[144] Let us now find an equilibrium solution across the fluid interface and calculate an interfacial tension per unit length of the interface. It is instructive to compare the numerical solution one can obtain with the LBM algorithm with the respective analytical solution. An exact analytical solution of the order parameter distribution across the fluid interface is found analytically by solving the equation $\mu = 0$ in one dimension across the interface. This solution reads

$$\phi_{\mathrm{eq}} = \sqrt{\frac{a}{b}} \tanh \frac{(x - x_0)}{\sqrt{2}\xi} \qquad [111]$$

where x_0 marks the center of the interface, and $\xi = \sqrt{\kappa/a}$ defines the interface thickness. From Eq. [111], the order parameter varies from $-\sqrt{a/b}$ for the pure A phase to $+\sqrt{a/b}$ for the pure B phase. For simplicity, in most simulation studies one typically lets b to be equal to a so that the order parameter varies from "-1" to "+1." The interfacial tension of the system per unit length of the interface is defined as an integral of the total energy over the entire width of the interface (perpendicular to the interface). Thereby, to calculate the interfacial tension in our system, we integrate over the interface width assuming that the coordinate x is in the direction normal to the fluid interface, and setting the origin of the coordinate system to the center of the interface between the two phases so that $x_0 = 0$. Integrating across the interface width in one dimension and taking into account the above equilibrium solution from Eq. [111], we find the interfacial tension

$$\sigma = \int_{-\infty}^{+\infty} dx \left[-\frac{a}{2}\phi_{\mathrm{eq}}^2(x) + \frac{b}{4}\phi_{\mathrm{eq}}^4(x) - \frac{\kappa}{2}\left(\partial_x \phi_{\mathrm{eq}}(x)\right)^2 \right] = \sqrt{\frac{8\kappa a^3}{9b^2}} \qquad [112]$$

One can also show[3] that the two contributions to the total energy in Eq. [112], that from the local, bulk free energy (first two terms), and that from the gradient terms, are equal. The LBM formulation effectively allows us to find the numerical solution of the above system of equations with the given boundary conditions.

In the multiphase LBM, the physical variables (density, order parameter, and velocity) are defined through the two sets of distribution functions that are discrete in space and time (to be shown below), which differs from the single set of distribution functions discussed earlier. We now mainly focus on the binary fluid with the same densities and viscosities for the fluid phases and on the single relaxation time approach for these systems, but we will also comment on the extension of this approach to the MRT scheme at the end of this section. Finally, we note that this formulation can be extended in a straightforward manner to model the behavior of ternary fluids. In this case, the total free energy of the system needs to be extended to the triple-well potential, where each of the potential minima corresponds to one of the three fluid phases and the interfacial energies need to be defined between all components within the system.[160–162]

Lattice Boltzmann Algorithm for Binary Fluid: Free-Energy Approach

Similar to the single component LBM approach, LBM simulations for multicomponent fluids consist of two steps: a collision step and a streaming step. During the collision step, the particles of two types undergo collision at each lattice site of the regular lattice. During the streaming step, these particles propagate to the neighboring sites. In two dimensions, one often uses the nine velocities or D2Q9 model. This nine-velocity model is defined in two dimensions with velocity vectors $\mathbf{e}_i = (\pm 1,0), (0, \pm 1), (\pm 1, \pm 1), (0,0)$. These dimensionless velocity vectors are related to the dimensional velocity vectors defined in the previous section as $\mathbf{c}_i = a_s \mathbf{e}_i a/h$ where $a_s = \sqrt{3}$. The formalism applies similarly in three dimensions and later we will refer to examples using a D3Q19 model. We will keep notations throughout this section in the same format as is typically introduced in the free-energy LBM literature.[5,143,145,163]

For the binary fluid, two distribution functions are defined on a regular lattice, $f_i(\mathbf{x})$ and $g_i(\mathbf{x})$ on each lattice site $\mathbf{x}$. The conserved physical variables (density $\rho(\mathbf{x}, t)$, momentum $\mathbf{j}(\mathbf{x},t) = \rho(\mathbf{x},t)\mathbf{u}(\mathbf{x},t)$, and order parameter $\phi(\mathbf{x}, t)$) are calculated through these distribution functions as:

$$\rho = \sum_i f_i, \quad \rho u_\alpha = \sum_i f_i e_{i\alpha}, \quad \phi = \sum_i g_i \qquad [113]$$

The time evolution equation for these two-particle distribution functions are calculated during the collision and streaming steps. During the collision step, the values of the distribution functions are updated based on the collision operators on the right-hand side of Eqs. [114] and [115] (here, we will only use the BGK approximation)

$$f_i^*(\mathbf{x},t) = f_i(\mathbf{x},t) - \frac{f_i - f_i^{\mathrm{eq}}}{\tau_\rho} \qquad [114]$$

and

$$g_i^*(\mathbf{x},t) = f_i(\mathbf{x},t) - \frac{g_i - g_i^{\mathrm{eq}}}{\tau_\phi} \quad [115]$$

where τ_ρ and τ_ϕ are the respective relaxation times. The streaming step that follows the collision step moves the particles along the corresponding lattice velocity directions, $\mathbf{e}_i$, as

$$f_i(\mathbf{x} + \mathbf{e}_i\Delta x, t + \Delta t) = f_i^*(\mathbf{x},t) \quad [116]$$

and

$$g_i(\mathbf{x} + \mathbf{e}_i\Delta x, t + \Delta t) = g_i^*(\mathbf{x},t) \quad [117]$$

The functions f_i^{eq} and g_i^{eq} in the above equations denote the corresponding equilibrium distribution functions. These functions can be defined as power series in the local velocity and within the free-energy LBM approach are written as

$$f_i^{\mathrm{eq}} = A_s + B_s e_{i\alpha}u_\alpha + C_s u^2 + D_s e_{i\alpha}e_{i\beta}u_\alpha u_\beta + G_{s\alpha\beta}e_{i\alpha}e_{i\beta} \quad [118a]$$

$$g_i^{\mathrm{eq}} = H_s + K_s e_{i\alpha}u_\alpha + J_s u^2 + Q_s e_{i\alpha}e_{i\beta}u_\alpha u_\beta \quad [118b]$$

where the index s allows one to choose different coefficients depending on the length of the velocity vector, e_i. This index s takes the following values $s = \in \{0,1,2\}$ for the velocity vector length of $0,1,\sqrt{2}$, respectively. The coefficients in Eqs. [118a] and [118b] can be found by requiring that the equilibrium distribution functions satisfy the following constraints. First, the conservation of density of each component and the conservation of fluid momentum are imposed as

$$\sum_i f_i^{\mathrm{eq}} = \rho, \quad \sum_i f_i^{\mathrm{eq}} e_{i\alpha} = \rho u_\alpha, \quad \sum_i g_i^{\mathrm{eq}} = \phi \quad [119]$$

In addition, the following constraints are also imposed so that the continuum equations above are satisfied[143–145]

$$\sum_i f_i^{\mathrm{eq}} e_{i\alpha}e_{i\beta} = P_{\alpha\beta} + \rho u_\alpha u_\beta \quad [120a]$$

$$\sum_i g_i^{\mathrm{eq}} e_{i\alpha} = \phi u_\alpha \quad [120b]$$

$$\sum_i g_i^{\mathrm{eq}} e_{i\alpha}e_{i\beta} = \Gamma\mu\delta_{\alpha\beta} + \phi u_\alpha u_\beta \quad [120c]$$

where Γ is a model parameter that allows one to define the mobility of the order parameter as[143,144]

$$M = \Delta t \Gamma \left(\tau_\phi - \frac{1}{2} \right) \quad [121]$$

One can show[143,145] that the continuum equations [104a], [104b], and [104c] are satisfied if an appropriate choice is made of the coefficients in the expansion in Eqs. [118a] and [118b].We note that an additional term on the right-hand side of Eq. [104b] arises as a result of such expansion but this term is typically significantly smaller than the other terms.[144,145] The Navier–Stokes equation is satisfied if the kinematic viscosity for binary fluid is defined as,[143,163] cf. Eq. [49a],

$$\nu = \Delta t \frac{c^2}{3} \left(\tau_\rho - \frac{1}{2} \right) \quad [122]$$

An example of a set of coefficients for the expansions in Eqs.[118a] and [118b] that satisfies all the above constraints is given in Ref. 144 and an explanation of how one can derive these coefficients is given in Ref. 143.

We emphasize here that the coefficients in Eqs. [118a] and [118b] are not constant values. Instead, these are parameters that depend on either local parameters (fluid density or order parameter) or on the gradients. Therefore, these coefficients are recalculated at each LB time step when calculating new values for the collision operator. For example, all A_s and G_s in the above expansion for the equilibrium functions depend on the pressure tensor, and H_s are calculated based on the values of the chemical potential at the given lattice site, μ.[144] The accuracy of calculating the gradients is critically important, because, to a large extent, it affects the accuracy of the LBM approach. Finally, we comment here on the relationship between the experimental values that describe the system of interest and the respective dimensionless simulation parameters. The corresponding characteristic length scale and timescales could be expressed through the experimental parameters as[164] $L_0 = \eta^2/\rho\sigma$ and $T_0 = \eta^3/\rho\sigma^2$. Here, the value of σ denotes experimental values of an interfacial tension, whereas its dimensionless simulation value is derived from Eq. [112]. Along with the dimensionless numbers discussed in the previous section, a capillary number $Ca = \eta u/\sigma$ is often used to characterize the ratio of viscous and interfacial forces. We emphasize that the LBM is a mesoscale approach and is typically used to simulate the dynamics of fluid systems on the micron to millimeter-scale; hence, the lattice resolution Δx is usually chosen on the order of microns to millimeters. Importantly, as we noted earlier, the interface width has to occupy multiple lattice sites such that the width of the interface defined above can reach tens to hundreds of microns, which is a few orders of magnitude greater than the width of the interface between the immiscible fluids in experimental systems (on the order of nanometers). However, by accurately accounting for

the correct interfacial tension in the system, the physics of a number of interfacial phenomena can be accurately represented, including dynamics of the contact line motion, imbibition processes, as well as droplet dynamics on patterned and structured surfaces. Some scaling issues that arise in more complex multicomponent binary systems that include colloidal particles are discussed in detail in Ref. 164.

Examples of LBM Simulations in 2D and 3D We now provide a few examples of LBM free-energy simulations in two and three dimensions. Figure 7 depicts a phase separation under the shear flow in a binary fluid in two dimensions[152] (D2Q9 grid was used). Here, the simulations start from the initially homogeneous 50/50 mixture (50% of an A phase and a 50% of a B phase within the fluid mixture), quenched into the immiscible region. The shear flow results in the anisotropic elongation of the domains along the flow direction (horizontal direction in this figure) affecting the domain growth.[152] The domain growth in Figure 7 is seen from white and dark domains corresponding to the different phases as phase separation takes place.

Figures 8 and 9 are examples illustrating that the multiphase free-energy LBM approach can solve various problems involving interactions between droplets and structured surfaces. In both cases, 3D liquid–gas free energy LBM was used by Yeomans et al.[165,166] and the wetting conditions (contact angle) between the liquid and the substrates are implemented as described above. We specifically selected these two cases as examples where LBM simulation results are compared to the respective experimental studies. Modeling can reproduce the main features of a process of evaporation of the microscale droplet on the topologically structured surfaces,[165] as can be seen from Figure 8. In the second example,[167] the evolution of the shape of a spherical droplet during its impact on a superhydrophobic surface is considered in both LBM simulations and in experiments. The image in Figure 9 illustrates an example of "pancake" bouncing. The droplet shape transitions resemble that in the experiment:[166] it was shown that the type of the droplet bouncing depends on the Weber number $We = \rho v_{\text{imp}}^2 R/\sigma$. This number gives a ratio of the inertial energy to the surface tension energy, where v_{imp} is an impact velocity, R is a droplet radius, and σ is the surface tension. These simulations were carried out on a regular D3Q19 grid (cf. Figure 1), however, the droplet was not spherical.

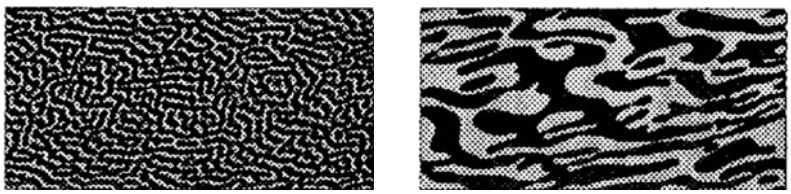

FIGURE 7 Phase separation in the shear flows (directed from the left to the right). *Source*: reprinted with permission from Ref. 152. Copyright (1999) by the American Physical Society.

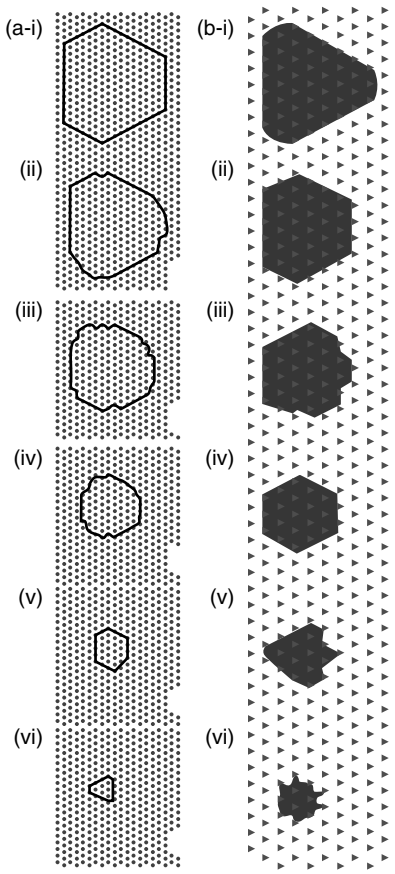

FIGURE 8 Contact line dynamics during droplet evaporation on surfaces patterned with triangular posts on a hexagonal lattice observed in experiments (left column) and LBM simulations (right column). *Source*: reproduced from Ref. 165 with permission of The Royal Society of Chemistry. (See color plate section for the color representation of this figure.)

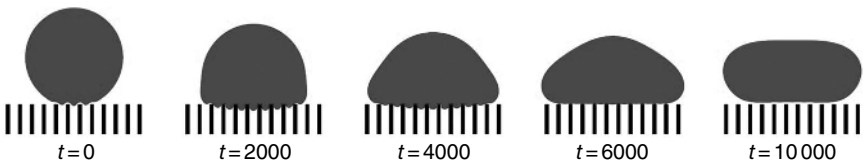

FIGURE 9 LBM simulations of a "pancake bouncing" of a liquid droplet on a structured surface. *Source*: reprinted with permission from Ref. 166. Copyright (2014) American Chemical Society.

Instead, it was a cylindrical droplet in 3D, which represents a suitable compromise between the full 3D simulations of a droplet spreading and a simple 2D modeling of a 2D droplet cross-section. The limitations of the LBM approach to simulate this system along with remaining open questions are also discussed in Ref. 166. It was pointed out, for example, that the density and viscosity of the gas were taken to have significantly higher values than the corresponding experimental values due to stability issues (which is typical for this class of models), and that the average Reynolds numbers in the simulations were significantly smaller than that in experiments.[166] Despite these limitations, the simulations provide useful insight into the behavior of a bouncing droplet on structured surfaces. We also note that, in the latter case, the MRT collision model was used, a point we will return to at the end of this section. The behavior of liquid droplets impacting solid surfaces are important for many applications, from ink-jet printing to crop spraying, and simulations can help us to understand key features of these processes.

Minimizing Spurious Velocities

A well-known issue in simulating fluids using multiphase LBM techniques is the existence of unphysical flows near the interfaces when the system reaches an equilibrium. These flows are referred to as "spurious currents" or "spurious velocities," the magnitude of which depends on the specifics of the LBM implementations, on the chosen equilibrium distribution functions, surface tension, viscosity, and on the curvature of the interface. Here, we review the spurious velocities appearing in the free-energy LBM. For comparison of spurious velocities in other multiphase LBM approaches, we refer the reader to a recent review[167] and references therein.

An example of the spurious velocity field around a liquid droplet in equilibrium with its vapor phase is shown in Figure 10a. The simulations in this image were conducted using the standard free-energy lattice-gas LBM approach.[5] The density field within the droplet is higher than outside and corresponds to the liquid phase. This density is set at 4.54 in the given example and that of the outer vapor phase is 2.57.[163] The ratio between the densities of the two phases is typically rather small (on the order of 10); this is a common feature of this class of models. The size of the arrows in Figure 10 corresponds to the magnitude of the velocity so that one can clearly see that the maximum spurious velocities appear at the droplet interface. The flow field forms eight vortices and the maximum magnitude of the spurious velocities are on the order of $10^{-5}c$ to $10^{-4}c$.[164] Ideally, however, these velocities should vanish to machine precision when the system reaches an equilibrium and is at rest in the absence of thermal fluctuations.

Similar spurious velocities are observed in binary fluid simulations, not only in the case of the liquid–gas system. An example of the distribution of the spurious velocity field for a droplet of fluid A within fluid B is given in Ref. 168. The density of the fluid changes across a few lattice sites across the interfacial region according to Eq. [111] from the value close to "-1" within the center of the droplet

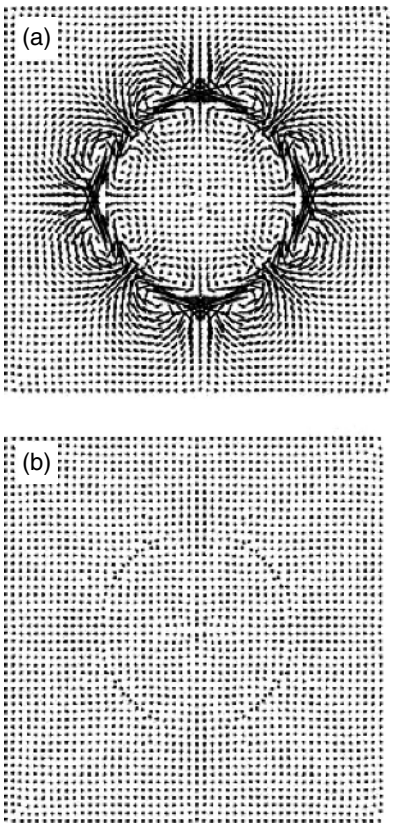

FIGURE 10 Spurious velocities around the liquid droplet in equilibrium with its vapor (a) using standard free-energy LBM approach, and (b) using modified approached that minimizes spurious velocities. *Source*: reprinted with permission from Ref. 163. Copyright (2008) by the American Physical Society.

to the value close to "+1" in the outer region. The spurious velocities again form eight vortices around the droplet in the outer phase, and the velocity profile closely resembles the profile shown in Figure 10a. Notably, the distribution of μ also remains nonuniform in equilibrium.[168]

A number of studies have focused on minimizing spurious velocities in multiphase LBM systems.[167–171] For purely diffusive systems, where one essentially needs to integrate only the Cahn–Hilliard equation without the hydrodynamics taken into account (so-called Model B),[142] Wagner have shown that the LBM approach can be reformulated with the spurious velocities reduced to machine precision.[168] Furthermore, it was shown that spurious velocities will reappear in the same system when HI are reintroduced, yet they can be reduced almost to machine precision by modifying the forcing term in the Navier–Stokes equation. However,

this reduction came at a cost: momentum was no longer conserved and the method was no longer stable unless additional corrections in viscosity were applied.[168]

A significant reduction in the magnitude of spurious velocities was achieved by Pooley and Furdato[163] for both liquid–gas and binary fluid systems by means of optimal choice of stencils for calculating the gradients and the Laplacian in combination with optimizing the equilibrium distribution functions. Recall that stencil sets an arrangement of a neighboring nodal group with relation to the point at which a derivative is taken. The justification of the optimal choice of the stencils for the gradient and Laplacian is given in Ref. 163. For example, a conventional two-point representation for the gradient along the x-direction

$$\partial_x = \frac{1}{2\Delta x}\begin{bmatrix} 0 & 0 & 0 \\ -1 & 0 & 1 \\ 0 & 0 & 0 \end{bmatrix} \qquad [123]$$

where the central entry in the matrix represents the point at which the derivative is taken and the surrounding points represent neighboring lattice points, was replaced with

$$\partial_x = \frac{1}{12\Delta x}\begin{bmatrix} -1 & 0 & 1 \\ -4 & 0 & 4 \\ -1 & 0 & 1 \end{bmatrix} \qquad [124]$$

and the optimal choice for the Laplacian in terms of minimizing spurious velocities reads:[163]

$$\nabla^2 = \frac{1}{6\Delta x^2}\begin{bmatrix} 1 & 4 & 1 \\ 4 & -20 & 4 \\ 1 & 4 & 1 \end{bmatrix} \qquad [125]$$

The above choices improve the isotropy of calculating these operators and lead to reduced spurious velocities. In addition, modifications to the equilibrium distribution functions were made to reduce the spurious velocities.[163]

These choices resulted in numerically stable schemes that did not sacrifice momentum conservation. While the spurious velocities were not reduced to machine precision, they were reduced significantly and for the system with the same parameters as in Figure 10a an improved approach resulted in the profile shown in Figure 10b. In addition to the spurious velocities appearing at the interfaces, similar spurious velocities also appear at the bounding surfaces, for example, when simulating the contact line dynamics along the surface. It was shown that, if the viscosities of both phases are chosen to be equal, the standard single relaxation

time multiphase LBM can be used to simulate the contact line dynamics with high accuracy.[149,159,172] However, in many fundamentally and technologically relevant problems, one needs to focus on the binary fluid with both fluids having distinctly different viscosities. To account for the difference in fluid viscosities as well as to minimize spurious velocities appearing at the surfaces, the single relaxation time collision operator needs to be replaced with a multiple relaxation time collision operator in Eq. [114][173] The single relaxation time collision operator in Eq. [115] does not contribute to an increase in magnitude of the spurious velocities.[173] A simulation of a capillary filling, when a fluid is pulled into a hydrophilic capillary by the Laplace pressure across the interface, was performed to test the accuracy of the proposed MRT multiphase LBM. It was shown that the length of fluid within the capillary obeys Washburn's law closely for a range of capillary numbers, confirming the applicability of this approach.[173] We note that the MRT approach for multiphase binary fluid had been used in the 3D LBM simulations that we referred to earlier, cf. Figure 9. Finally, we note that the free-energy multiphase LBM approaches for lattice-gas systems are applicable for small density ratios only. There are different LBM formulations that focus on simulations of high-density ratio fluids.[174–176] With respect to spurious velocities, the magnitudes and the distribution of these velocities were calculated for a number of density ratios up to 1 : 1000 between the two phases in Ref. 175. For the highest density ratio, the maximum spurious velocities reached $3{\cdot}10^{-2}$ at the interfaces.

CONCLUSIONS

This tutorial-review is an introduction to the LBM for both single-component and multiphase fluids. When introducing the LBM for single-phase fluids, we focused on the development of lattice models based on the underlying kinetic theory. The systematic derivation unveils the approximations that are connected to the limits of small Mach and small Knudsen number where the LBM reproduces the incompressible Navier–Stokes equations. Moreover, the derivation reveals the orders of the discretization errors and the sources of potential instabilities. We hope that an understanding of these connections will enable the reader to chose a proper simulation setup when using the LBM. Boundary conditions and thermal fluctuations are essential requirements for simulating the behavior of complex fluids, and we have provided an overview of the most important developments. The prototype systems for which these approaches have been developed are colloidal dispersions and polymer solutions. Many other soft matter systems have been investigated, and new extensions of the method are under active development.[55] Recent advances include the ability to simulate electrokinetic phenomena in charged colloidal and polymeric systems.[121–123,125] Furthermore, boundary conditions and force coupling are not restricted to single phase fluids, and applications that combine them with multicomponent and multiphase systems are only beginning to emerge.[111,126]

When introducing the LBM approach for multiphase fluid, we focused primarily on the free-energy LBM approach, and only briefly discussed the history and application of other methods. We note here, however, that the development of multiphase algorithms remains active and typically aims to resolve issues that continue to pose challenges, such as modeling fluids with high-density ratios.[174–176] For example, in the most recent work,[176] the LBM with a weighed multiple relaxation collision model and with an adaptive mesh refinement algorithm was introduced to enhance numerical stability in three dimensions, specifically at high-density ratios.

With respect to the free-energy LBM approach, we provided a brief introduction and gave a few examples of using it in two and three dimensions to model various binary systems. We also discussed problematic issue in multiphase LBM that is an existence of spurious velocities around the interfaces between the phases and how these velocities could be minimized. It is also worth noting that the free-energy multiphase LBM approach has been adapted and used successfully in a number of even more complex systems, from liquid crystalline systems[177,178] to active nematic liquid crystals.[179–181] A recent study has shown,[181] for example, that epithelial tissue can be modeled as active nematic liquid crystals using an LBM approach. While we have focused here on binary fluids, multiphase LBM approaches have also been extended to model the behavior of ternary fluids.[160–162,182–184]

Overall, the LBM has enabled a host of applications in soft matter research. We anticipate that it will soon make inroads into significant innovations in materials design by opening up the opportunity to predict structure–property relations for soft materials and complex fluids. Hence, in our view, the LBM is a powerful and versatile tool in the virtual materials laboratory.

REFERENCES

1. B. Dünweg and A. J. C. Ladd, *Adv. Poly. Sci.*, **221**, 89 (2009). Lattice Boltzmann Simulations of Soft Matter Systems.
2. D. M. Anderson, G. B. McFadden, and A. A. Wheeler, *Annu. Rev. Fluid Mech.*, **30**, 139 (1998). Diffuse-Interface Methods in Fluid Mechanics.
3. P. Yue, J. J. Feng, C. Liu, and J. Shen, *J. Fluid Mech.*, **515**, 293 (2004). A Diffuse-Interface Method for Simulating Two-Phase Flows of Complex Fluids.
4. M. R. Swift, W. R. Osborn, and J. M. Yeomans, *Phys. Rev. Lett.*, **75**, 830 (1995). Lattice Boltzmann Simulation of Nonideal Fluids.
5. M. R. Swift, E. Orlandini, W. R. Osborn, and J. M. Yeomans, *Phys. Rev. E*, **54**, 5041 (1996). Lattice Boltzmann Simulations of Liquid-Gas and Binary Fluid Systems.
6. A. K. Gunstensen, D. H. Rothman, S. Zaleski, and G. Zanetti, *Phys. Rev. A*, **43**, 4320 (1991). Lattice Boltzmann Model of Immiscible Fluids.
7. X. W. Shan and H. D. Chen, *Phys. Rev. E*, **47**, 1815 (1993). Lattice Boltzmann Model for Simulating Flows with Multiple Phases and Components.

8. X. W. Shan and H. D. Chen, *Phys. Rev. E*, **49**, 2941 (1994). Simulation of Nonideal Gases and Liquid-Gas Phase-Transitions by the Lattice Boltzmann Equation.
9. S. Chen and G. D. Doolen, *Annu. Rev. Fluid Mech.*, **30**, 329 (1998). Lattice Boltzmann Method for Fluid Flows.
10. C. K. Aidun and J. R. Clausen, *Annu. Rev. Fluid Mech.*, **42**, 439 (2010). Lattice-Boltzmann Method for Complex Flows.
11. J. Yang and E. S. Boek, *Comput. Math. Appl.*, **65**, 882 (2013). A Comparison Study of Multi-Component Lattice Boltzmann Models for Flow in Porous Media Applications. Mesoscopic Methods in Engineering and Science.
12. Q. Li, K. Luo, Q. Kang, Y. He, Q. Chen, and Q. Liu, *Prog. Energy Combust. Sci.*, **52**, 62 (2016). Lattice Boltzmann Methods for Multiphase Flow and Phase-Change Heat Transfer.
13. S. Chapman and T. G. Cowling, *The Mathematical Theory of Non-Uniform Gases*. Cambridge Mathematical Library Series, 3rd ed., Cambridge University Press, Cambridge, UK, 1990.
14. S. Wolfram, *J. Stat. Phys.*, **45**, 471 (1986). Cellular Automaton Fluids 1: Basic Theory.
15. U. Frisch, D. d'Humières, B. Hasslacher, P. Lallemand, Y. Pomeau, and J.-P. Rivet, *Complex Syst.*, **1**, 649 (1987). Lattice Gas Hydrodynamics in Two and Three Dimensions.
16. D. A. Wolf-Gladrow, *Lattice-Gas Cellular Automata and Lattice Boltzmann Models*. Springer, Berlin, 2000.
17. L. P. Kadanoff and J. Swift, *Phys. Rev.*, **165**, 310 (1968). Transport Coefficients Near the Critical Point: A Master-Equation Approach.
18. J. Hardy, Y. Pomeau, and O. de Pazzis, *J. Math. Phys.*, **14**, 1746 (1973). Time Evolution of a Two-Dimensional Model System. I. Invariant States and Time Correlation Functions.
19. U. Frisch, B. Hasslacher, and Y. Pomeau, *Phys. Rev. Lett.*, **56**, 1505 (1986). Lattice-Gas Automata for the Navier-Stokes Equation.
20. D. d'Humières, P. Lallemand, and U. Frisch, *Europhys. Lett.*, **2**, 291 (1986). Lattice Gas Models for 3D Hydrodynamics.
21. R. Benzi, S. Succi, and M. Vergalossa, *Phys. Rep.*, **222**, 145 (1992). The Lattice Boltzmann Equation: Theory and Applications.
22. G. McNamara and G. Zanetti, *Phys. Rev. Lett.*, **61**, 2332 (1988). Use of the Boltzmann Equation to Simulate Lattice-Gas Automata.
23. F. J. Higuera and J. Jimenez, *Europhys. Lett.*, **9**, 663 (1989). Boltzmann Approach to Lattice Gas Simulations.
24. P. L. Bhatnagar, E. P. Gross, and M. Krook, *Phys. Rev.*, **94**, 511 (1954). A Model for Collision Processes in Gases. I. Small Amplitude Processes in Charged and Neutral One-Component Systems.
25. J. M. Koelman, *Europhys. Lett.*, **15**, 603 (1991). A Simple Lattice Boltzmann Scheme for Navier-Stokes Fluid Flow.
26. S. Chen, H. Chen, D. Martinez, and W. Matthaeus, *Phys. Rev. Lett.*, **67**, 3776 (1991). Lattice Boltzmann Model for Simulation of Magnetohydrodynamics.
27. Y. H. Qian, D. d'Humières, and P. Lallemand, *Europhys. Lett.*, **17**, 479 (1992). Lattice BGK Models for Navier-Stokes Equation.

28. S. Succi, *The Lattice Boltzmann Equation for Fluid Dynamics and Beyond*. Clarendon Press, Oxford, 2001.
29. D. d'Humières, *Rarefied Gas Dynamics: Theory and Simulations*, B. D. Shizgal and D. P. Weaver, Eds., volume 159 of *Progress in Astronautics and Aeronautics*, 1992, pp. 450–458. Generalized Lattice-Boltzmann Equations. American Institute of Aeronautics and Astronautics, Inc., Reston, VA.
30. D. d'Humières, M. Bouzidi, and P. Lallemand, *Phys. Rev. E*, **63**, 066702 (2001). Thirteen-Velocity Three-Dimensional Lattice Boltzmann Model.
31. D. d'Humières, I. Ginzburg, M. Krafczyk, P. Lallemand, and L.-S. Luo, *Philos. Trans. R. Soc. Lond. A*, **360**, 437 (2002). Multiple-relaxation Time Lattice Boltzmann Models in Three Dimensions.
32. P. Lallemand and L.-S. Luo, *Phys. Rev. E*, **61**, 6546 (2000). Theory of the Lattice Boltzmann Method: Dispersion, Dissipation, Isotropy, Galilean Invariance, and Stability.
33. X. He and L.-S. Luo, *Phys. Rev. E*, **55**, R6333 (1997). *A Priori* Derivation of the Lattice Boltzmann Equation.
34. X. He and L.-S. Luo, *Phys. Rev. E*, **56**, 6811 (1997). Theory of the Lattice Boltzmann Method: From the Boltzmann Equation to the Lattice Boltzmann Equation.
35. X. Shan and X. He, *Phys. Rev. Lett.*, **80**, 65 (1998). Discretization of the Velocity Space in the Solution of the Boltzmann Equation.
36. X. Shan, X.-F. Yuan, and H. Chen, *J. Fluid. Mech.*, **550**, 413 (2006). Kinetic Theory Representation of Hydrodynamics: A Way Beyond the Navier-Stokes Equation.
37. A. J. Wagner, *Europhys. Lett.*, **44**, 144 (1998). An *H*-Theorem for the Lattice Boltzmann Approach to Hydrodynamics.
38. I. V. Karlin, A. N. Gorban, S. Succi, and V. Boffi, *Phys. Rev. Lett.*, **81**, 6 (1998). Maximum Entropy Principle for Lattice Kinetic Equations.
39. I. V. Karlin and S. Succi, *Phys. Rev. E*, **58**, R4053 (1998). Equilibria for Discrete Kinetic Equations.
40. I. V. Karlin, A. Ferrante, and H. C. Öttinger, *Europhys. Lett.*, **47**, 182 (1999). Perfect Entropy Functions of the Lattice Boltzmann Method.
41. S. Ansumali and I. V. Karlin, *Phys. Rev. E*, **62**, 7999 (2000). Stabilization of the Lattice Boltzmann Method by the *H* Theorem: A Numerical Test.
42. S. Succi, I. V. Karlin, and H. Chen, *Rev. Mod. Phys.*, **74**, 1203 (2002). *Colloquium*: Role of the *H* Theorem in Lattice Boltzmann Hydrodynamic simulations.
43. R. Adhikari, K. Stratford, M. E. Cates, and A. J. Wagner, *Europhys. Lett.*, **71**, 473 (2005). Fluctuating Lattice Boltzmann.
44. B. Dünweg, U. D. Schiller, and A. J. C. Ladd, *Phys. Rev. E*, **76**, 036704 (2007). Statistical Mechanics of the Fluctuating Lattice Boltzmann Equation.
45. B. Dünweg, U. D. Schiller, and A. J. Ladd, *Comput. Phys. Comm.*, **180**, 605 (2009). Progress in the Understanding of the Fluctuating Lattice Boltzmann Equation.
46. P. C. Philippi, L. A. Hegele, L. O. E. dos Santos, and R. Surmas, *Phys. Rev. E*, **73**, 056702 (2006). From the Continuous to the Lattice Boltzmann equation: The Discretization Problem and Thermal Models.
47. D. N. Siebert, L. A. Hegele, and P. C. Philippi, *Phys. Rev. E*, **77**, 026707 (2008). Lattice Boltzmann Equation Linear Stability Analysis: Thermal and Athermal Models.

48. K. K. Mattila, L. A. Hegele, and P. C. Philippi, *Phys. Rev. E*, **91**, 063010 (2015). Investigation of an Entropic Stabilizer for the Lattice-Boltzmann Method.
49. A. J. C. Ladd, *Phys. Rev. Lett.*, **70**, 1339 (1993). Short-time Motion of Colloidal Particles—Numerical Simulation via a Fluctuating Lattice-Boltzmann Equation.
50. A. J. C. Ladd, *J. Fluid Mech*., **271**, 285 (1994). Numerical Simulations of Particulate Suspensions via a Discretized Boltzmann Equation. Part 1. Theoretical Foundation.
51. A. J. C. Ladd, *J. Fluid Mech.*, **271**, 311 (1994). Numerical Simulations of Particulate Suspensions via a Discretized Boltzmann Equation. Part 2. Numerical Results.
52. P. Ahlrichs and B. Dünweg, *Int. J. Mod. Phys. C*, **9**, 1429 (1998). Lattice Boltzmann Simulation of Polymer-Solvent Systems.
53. P. Ahlrichs and B. Dünweg, *J. Chem. Phys.*, **111**, 8225 (1999). Simulation of a Single Polymer Chain in Solution by Combining Lattice Boltzmann and Molecular Dynamics.
54. P. Ahlrichs, R. Everaers, and B. Dünweg, *Phys. Rev. E*, **64**, 040501 (2001). Screening of Hydrodynamic Interactions in Semidilute Polymer Solutions: A Computer Simulation Study.
55. J. Zelko and B. Dünweg, *arXiv*, 1402.2920 (2014). Consistent Two-Phase Lattice Boltzmann Model for Gas-Liquid Systems. arXiv: 1402.2920.
56. C. Cercignani, *The Boltzmann Equation and Its Applications*, volume 67 of *Applied Mathematical Sciences*. Springer, New York, 1988.
57. J. C. Maxwell, *Philos. Trans. R. Soc. Lond.*, **157**, 49 (1867). On the Dynamical Theory of Gases.
58. L. Boltzmann, *Sitzungsberichte der Akademie der Wissenschaften zu Wien*, **66**, 275 (1872).
59. E. P. Gross and E. A. Jackson, *Phys. Fluids*, **2**, 432 (1959). Kinetic Models and the Linearized Boltzmann Equation.
60. H. Grad, *Comm. Pure Appl. Math.*, **2**, 325 (1949). Note on *N*-Dimensional Hermite Polynomials.
61. H. Grad, *Comm. Pure Appl. Math.*, **2**, 331 (1949). On the Kinetic Theory of Rarified Gases.
62. J. E. Broadwell, *J. Fluid Mech.*, **19**, 401 (1964). Study of Rarefied Shear Flow by the Discrete Velocity Method.
63. L.-S. Luo, *Comput. Phys. Commun.*, **129**, 63 (2000). Some Recent Results on Discrete Velocity Models and Ramifications for Lattice Boltzmann Equation.
64. U. D. Schiller. *Thermal Fluctuations and Boundary Conditions in the Lattice Boltzmann Method*. PhD thesis, Johannes Gutenberg University Mainz, 2008.
65. X. B. Nie, X. Shan, and H. Chen, *Europhys. Lett.*, **81**, 34005 (2008). Galilean Invariance of Lattice Boltzmann Models.
66. D. N. Siebert, L. A. Hegele, R. Surmas, L. O. E. Dos Santos, and P. C. Philippi, *Int. J. Mod. Phys. C*, **18**, 546 (2007). Thermal Lattice Boltzmann in two Dimensions.
67. S. S. Chikatamarla and I. V. Karlin, *Phys. Rev. E*, **79**, 046701 (2009). Lattices for the Lattice Boltzmann Method.
68. L.-S. Luo, W. Liao, X. Chen, Y. Peng, and W. Zhang, *Phys. Rev. E*, **83**, 056710 (2011). Numerics of the Lattice Boltzmann Method: Effects of Collision Models on the Lattice Boltzmann Simulations.

69. X. He, X. Shan, and G. D. Doolen, *Phys. Rev. E*, **57**, R13 (1998). Discrete Boltzmann Equation Model for Nonideal Gases.
70. P. J. Dellar, *Comput. Math. Appl.*, **65**, 129 (2013). An Interpretation and Derivation of the Lattice Boltzmann Method Using Strang splitting.
71. U. D. Schiller, *Comput. Phys. Commun.*, **185**, 2586 (2014). A Unified Operator Splitting Approach for Multi-Scale Fluid-Particle Coupling in the Lattice Boltzmann Method.
72. P. J. Dellar, *J. Comput. Phys.*, **190**, 351 (2003). Incompressible Limits of Lattice Boltzmann Equations Using Multiple Relaxation Times.
73. P. J. Dellar, *Phys. Rev. E*, **64**, 031203 (2001). Bulk and Shear Viscosities in Lattice Boltzmann Equations.
74. A. J. C. Ladd and R. Verberg, *J. Stat. Phys.*, **104**, 1191 (2001). Lattice-Boltzmann Simulations of Particle-Fluid Suspensions.
75. I. Ginzburg and D. d'Humières, *Phys. Rev. E*, **68**, 066614 (2003). Multireflection Boundary Conditions for Lattice Boltzmann Models.
76. B. Chun and A. J. C. Ladd, *Phys. Rev. E*, **75**, 066705 (2007). Interpolated Boundary Condition for Lattice Boltzmann Simulations of Flows in Narrow Gaps.
77. J. Latt and B. Chopard, *Math. Comput. Simul.*, **72**, 165 (2006). Lattice Boltzmann Method with Regularized Pre-Collision Distribution Functions.
78. R. Zhang, X. Shan, and H. Chen, *Phys. Rev. E*, **74**, 046703 (2006). Efficient Kinetic Method for Fluid Simulation Beyond the Navier-Stokes Equation.
79. A. Montessori, G. Falcucci, P. Prestininzi, M. La Rocca, and S. Succi, *Phys. Rev. E*, **89**, 053317 (2014). Regularized Lattice Bhatnagar-Gross-Krook Model for Two- and Three-Dimensional Cavity Flow Simulations.
80. R. A. Brownlee, A. N. Gorban, and J. Levesley, *Phys. Rev. E*, **75**, 036711 (2007). Stability and Stabilization of the Lattice Boltzmann Method.
81. R. A. Brownlee, J. Levesley, D. Packwood, and A. N. Gorban, *Progr. Comput. Phys.*, **3**, 31 (2013). Add-ons for Lattice Boltzmann Methods: Regularization, Filtering and Limiters.
82. I. V. Karlin, F. Bösch, and S. S. Chikatamarla, *Phys. Rev. E*, **90**, 031302 (2014). Gibbs' Principle for the Lattice-Kinetic Theory of Fluid Dynamics.
83. M. Geier, A. Greiner, and J. G. Korvink, *Eur. Phys. J. Spec. Top.*, **171**, 55 (2009). A Factorized Central Moment Lattice Boltzmann Method.
84. K. N. Premnath and S. Banerjee, *J. Stat. Phys.*, **143**, 747 (2011). On the Three-Dimensional Central Moment Lattice Boltzmann Method.
85. M. Geier, M. Schönherr, A. Pasquali, and M. Krafczyk, *Comput. Math. Appl.*, **70**, 507 (2015). The Cumulant Lattice Boltzmann Equation in Three Dimensions: Theory and Validation.
86. A. C. Maggs and V. Rossetto, *Phys. Rev. Lett.*, **88**, 196402 (2002). Local Simulation Algorithms for Coulomb Interactions.
87. I. Pasichnyk and B. Dünweg, *J. Phys. Condens. Matter*, **16**, S3999 (2004). Coulomb Interactions via Local Dynamics: A Molecular-Dynamics Algorithm.
88. A. M. Artoli, A. G. Hoekstra, and P. M. A. Sloot, *Int. J. Mod. Phys. C*, **14**, 835 (2003). Accelerated Lattice BGK Method for Unsteady Simulations Through Mach Number Annealing.

89. A. M. Artoli, A. G. Hoekstra, and P. M. A. Sloot, *Comput. Fluids*, **35**, 227 (2006). Optimizing Lattice Boltzmann Simulations for Unsteady Flows.
90. T. T. Pham, U. D. Schiller, J. R. Prakash, and B. Duenweg, *J. Chem. Phys.*, **131**, 164114 (2009). Implicit and Explicit Solvent Models for the Simulation of a Single Polymer Chain in Solution: Lattice Boltzmann vs Brownian Dynamics.
91. A. J. C. Ladd, *J. Chem. Phys.*, **93**, 3484 (1990). Hydrodynamic Transport Coefficients of Random Dispersions of Hard Spheres.
92. C. K. Aidun, Y. Lu, and E.-J. Ding, *J. Fluid Mech.*, **373**, 287 (1998). Direct Analysis of Particulate Suspensions with Inertia using the Discrete Boltzmann Equation.
93. A. J. C. Nguyen and N.-Q. Ladd, *Phys. Rev. E*, **66**, 046708 (2002). Lubrication Corrections for Lattice-Boltzmann Simulations of Particle Suspensions.
94. E. J. Ding and C. K. Aidun, *J. Stat. Phys.*, **112**, 685 (2003). Extension of the Lattice-Boltzmann Method for Direct Simulation of Suspended Particles near Contact.
95. J. Smiatek, M. P. Allen, and F. Schmid, *Eur. Phys. J. E*, **26**, 115 (2008). Tunable-Slip Boundaries for Coarse-Grained Simulations of Fluid Flow.
96. M. Sbragaglia and S. Succi, *Phys. Fluids*, **17**, 093602 (2005). Analytical Calculation of Slip Flow in Lattice Boltzmann Models with Kinetic Boundary Conditions.
97. R. Benzi, L. Biferale, M. Sbragaglia, S. Succi, and F. Toschi, *Europhys. Lett.*, **74**, 651 (2006). Mesoscopic Two-Phase Model for Describing Apparent Slip in Micro-Channel Flows.
98. M. Bouzidi, D. d'Humières, P. Lallemand, and L.-S. Luo, *J. Comput. Phys.*, **172**, 704 (2001). Lattice Boltzmann Equation on a Two-Dimensional Rectangular Grid.
99. M. Rohde, D. Kandhai, J. J. Derksen, and H. E. A. van den Akker, *Phys. Rev. E*, **67**, 066703 (2003). Improved Bounce-Back Methods for No-Slip Walls in Lattice-Boltzmann Schemes: Theory and Simulations.
100. P. A. Skordos, *Phys. Rev. E*, **48**, 4823 (1993). Initial and Boundary Conditions for the Lattice Boltzmann Method.
101. D. R. Noble, S. Chen, J. G. Georgiadis, and R. O. Buckius, *Phys. Fluids*, **7**, 203 (1995). A Consistent Hydrodynamic Boundary Condition for the Lattice Boltzmann Method.
102. Q. Zou and X. He, *Phys. Fluids*, **9**, 1591 (1997). On Pressure and Velocity Boundary Conditions for the Lattice Boltzmann BGK Model.
103. M. Hecht and J. Harting, *J. Stat. Mech. Theor. Exp.*, **2010**, P01018 (2010). Implementation of On-Site Velocity Boundary Conditions for D3Q19 Lattice Boltzmann Simulations.
104. A. J. C. Ladd, *Mol. Phys.*, **113**, 2531 (2015). Lattice-Boltzmann Methods for Suspensions of Solid Particles.
105. A. J. C. Ladd, *Phys. Fluids*, **9**, 491 (1997). Sedimentation of Homogeneous Suspensions of Non-Brownian Spheres.
106. A. Komnik, J. Harting, and H. J. Herrmann, *J. Stat. Mech.*, P12003 (2004). Transport Phenomena and Structuring in Shear Flow of Suspensions Near Solid Walls.
107. M. Hecht, J. Harting, T. Ihle, and H. J. Herrmann, *Phys. Rev. E*, **72**, 011408 (2005). Simulation of Claylike Colloids.
108. M. Hecht, J. Harting, M. Bier, J. Reinshagen, and H. J. Herrmann, *Phys. Rev. E*, **74**, 021403 (2006). Shear Viscosity of Claylike Colloids in Computer Simulations and Experiments.

109. M. Hecht, J. Harting, and H. J. Herrmann, *Int. J. Mod. Phys. C*, **18**, 501 (2007). Formation and Growth of Clusters in Colloidal Suspensions.

110. F. Jansen and J. Harting, *Phys. Rev. E*, **83**, 046707 (2011). From Bijels to Pickering Emulsions: A Lattice Boltzmann Study.

111. S. Frijters, F. Günther, and J. Harting, *Soft Matter*, **8**, 6542 (2012). Effects of Nanoparticles and Surfactant on Droplets in Shear Flow.

112. F. Günther, F. Janoschek, S. Frijters, and J. Harting, *Comput. Fluids*, **80**, 184 (2013). Lattice Boltzmann Simulations of Anisotropic Particles at Liquid Interfaces.

113. G. B. Davies, T. Krüger, P. V. Coveney, J. Harting, and F. Bresme, *Adv. Mater.*, **26**, 6715 (2014). Assembling Ellipsoidal Particles at Fluid Interfaces using Switchable Dipolar Capillary Interactions.

114. G. B. Davies, T. Krüger, P. V. Coveney, J. Harting, and F. Bresme, *Soft Matter*, **10**, 6742 (2014). Interface Deformations Affect the Orientation Transition of Magnetic Ellipsoidal Particles Adsorbed at Fluid-Fluid Interfaces.

115. R. W. Nash, R. Adhikari, and M. E. Cates, *Phys. Rev. E*, **77**, 026709 (2008). Singular Forces and Pointlike Colloids in Lattice Boltzmann Hydrodynamics.

116. A. J. C. Ladd, R. Kekre, and J. E. Butler, *Phys. Rev. E*, **80**, 036704 (2009). Comparison of the Static and Dynamic Properties of a Semiflexible Polymer Using Lattice Boltzmann and Brownian-Dynamics Simulations.

117. M. Fyta, S. Melchionna, E. Kaxiras, and S. Succi, *Multiscale Model. Simul.*, **5**, 1156 (2006). Multiscale Coupling of Molecular Dynamics and Hydrodynamics: Application to DNA Translocation Through a Nanopore.

118. O. B. Usta, A. J. C. Ladd, and J. E. Butler, *J. Chem. Phys.*, **122**, 094902 (2005). Lattice-Boltzmann Simulations of the Dynamics of Polymer Solutions in Periodic and Confined Geometries.

119. R. Kekre, J. E. Butler, and A. J. C. Ladd, *Phys. Rev. E*, **82**, 011802 (2010). Comparison of Lattice-Boltzmann and Brownian-Dynamics Simulations of Polymer Migration in Confined Flows.

120. R. Kekre, J. E. Butler, and A. J. C. Ladd, *Phys. Rev. E*, **82**, 050803 (2010). Role of Hydrodynamic Interactions in the Migration of Polyelectrolytes Driven by a Pressure Gradient and an Electric Field.

121. J. Smiatek, M. Sega, C. Holm, U. D. Schiller, and F. Schmid, *J. Chem. Phys.*, **130**, 244702 (2009). Mesoscopic Simulations of the Counterion-Induced Electro-Osmotic Flow: A Comparative Study.

122. K. Grass, U. Böhme, U. Scheler, H. Cottet, and C. Holm, *Phys. Rev. Lett.*, **100**, 096104 (2008). Importance of Hydrodynamic Shielding for the Dynamic Behavior of Short Polyelectrolyte Chains.

123. M. Kuron, G. Rempfer, F. Schornbaum, M. Bauer, C. Godenschwager, C. Holm, and J. d. Graaf, *J. Chem. Phys.*, **145**, 214102 (2016). Moving Charged Particles in Lattice Boltzmann-Based Electrokinetics.

124. S. Kesselheim, M. Sega, and C. Holm, *Soft Matter*, **8**, 9480 (2012). Effects of Dielectric Mismatch and Chain Flexibility on the Translocation Barriers of Charged Macromolecules Through Solid State Nanopores.

125. S. Kesselheim, W. Müller, and C. Holm, *Phys. Rev. Lett.*, **112**, 018101 (2014). Origin of Current Blockades in Nanopore Translocation Experiments.

126. M. Sega, M. Sbragaglia, S. S. Kantorovich, and A. O. Ivanov, *Soft Matter*, **9**, 10092 (2013). Mesoscale Structures at Complex Fluid-Fluid Interfaces: A Novel Lattice Boltzmann/Molecular Dynamics Coupling.

127. V. Lobaskin and B. Dünweg, *New J. Phys.*, **6**, 54 (2004). A New Model for Simulating Colloidal Dynamics.

128. V. Lobaskin, B. Dünweg, and C. Holm, *J. Phys. Condens. Matter*, **16**, S4063 (2004). Electrophoretic Mobility of a Charged Colloidal Particle: A Computer Simulation Study.

129. V. Lobaskin, B. Dünweg, M. Medebach, T. Palberg, and C. Holm, *Phys. Rev. Lett.*, **98**, 176105 (2007). Electrophoresis of Colloidal Dispersions in the Low-Salt Regime.

130. A. Chatterji and J. Horbach, *J. Chem. Phys.*, **122**, 184903 (2005). Combining Molecular Dynamics with Lattice Boltzmann: A Hybrid Method for the Simulation of (Charged) Colloidal Systems.

131. A. Chatterji and J. Horbach, *J. Chem. Phys.*, **126**, 064907 (2007). Electrophoretic Properties of Highly Charged Colloids: A Hybrid Molecular Dynamics/Lattice Boltzmann Simulation Study.

132. L. P. Fischer, T. Peter, C. Holm, and J. d. Graaf, *J. Chem. Phys.*, **143**, 084107 (2015). The Raspberry Model for Hydrodynamic Interactions Revisited. I. Periodic Arrays of Spheres and Dumbbells.

133. J. d. Graaf, T. Peter, L. P. Fischer, and C. Holm, *J. Chem. Phys.*, **143**, 084108 (2015). The Raspberry Model for Hydrodynamic Interactions Revisited. II. The Effect of Confinement.

134. R. M. MacMeccan, J. R. Clausen, G. P. Neitzel, and C. K. Aidun, *J. Fluid Mech.*, **618**, 13 (2009). Simulating Deformable Particle Suspensions Using a Coupled Lattice-Boltzmann and Finite-Element Method.

135. J. R. Clausen and C. K. Aidun, *Phys. Fluids*, **22**, 123302 (2010). Capsule Dynamics and Rheology in Shear Flow: Particle Pressure and Normal Stress.

136. J. Wu and C. K. Aidun, *Int. J. Numer. Meth. Fluids*, **62**, 765 (2010). Simulating 3D Deformable Particle Suspensions Using Lattice Boltzmann Method with Discrete External Boundary Force.

137. D. A. Reasor, J. R. Clausen, and C. K. Aidun, *Int. J. Numer. Meth. Fluids*, **68**, 767 (2011). Coupling the Lattice-Boltzmann and Spectrin-Link Methods for the Direct Numerical Simulation of Cellular Blood Flow.

138. S. K. Doddi and P. Bagchi, *Phys. Rev. E*, **79**, 046318 (2009). Three-Dimensional Computational Modeling of Multiple Deformable Cells Flowing in Microvessels.

139. T. Krüger, F. Varnik, and D. Raabe, *Comput. Method. Appl.*, **61**, 3485 (2011). Efficient and Accurate Simulations of Deformable Particles Immersed in a Fluid Using a Combined Immersed Boundary Lattice Boltzmann Finite Element Method.

140. T. Krüger, D. Holmes, and P. V. Coveney, *Biomicrofluidics*, **8**, 054114 (2014). Deformability-Based Red Blood Cell Separation in Deterministic Lateral Displacement Devices: A Simulation Study.

141. D. Goldstein, R. Handler, and L. Sirovich, *J. Comput. Phys.*, **105**, 354 (1993). Modeling a No-Slip Flow Boundary with an External Force Field.

142. A. J. Bray, *Adv. Phys.*, **51**, 481 (2002). Theory of Phase-Ordering Kinetics.

143. J. Yeomans, *Phy. A*, **369**, 159 (2006). Mesoscale Simulations: Lattice Boltzmann and Particle Algorithms. Fundamental Problems in Statistical Physics.

144. A. J. Briant and J. M. Yeomans, *Phys. Rev. E*, **69**, 031603 (2004). Lattice Boltzmann Simulations of Contact Line Motion. II. Binary Fluids.

145. A. J. Wagner. *Theory and Applications of the Lattice Boltzmann Method*. PhD thesis, University of Oxford, 1997.

146. D. Suppa, O. Kuksenok, A. C. Balazs, and J. M. Yeomans, *J. Chem. Phys.*, **116**, 6305 (2002). Phase Separation of a Binary Fluid in the Presence of Immobile Particles: A Lattice Boltzmann Approach.

147. R. Verberg, J. M. Yeomans, and A. C. Balazs, *J. Chem. Phys.*, **123**, 224706 (2005). Modeling the Flow of Fluid/Particle Mixtures in Microchannels: Encapsulating Nanoparticles Within Monodisperse Droplets.

148. R. Verberg, C. M. Pooley, J. M. Yeomans, and A. C. Balazs, *Phys. Rev. Lett.*, **93**, 184501 (2004). Pattern Formation in Binary Fluids Confined Between Rough, Chemically Heterogeneous Surfaces.

149. O. B. Usta, D. Perchak, A. Clarke, J. M. Yeomans, and A. C. Balazs, *J. Chem. Phys.*, **130**, 234905 (2009). Shear and Extensional Deformation of Droplets Containing Polymers and Nanoparticles.

150. Y. Ma, A. Bhattacharya, O. Kuksenok, D. Perchak, and A. C. Balazs, *Langmuir*, **28**, 11410 (2012). Modeling the Transport of Nanoparticle-Filled Binary Fluids through Micropores.

151. A. C. Balazs, R. Verberg, C. M. Pooley, and O. Kuksenok, *Soft Matter*, **1**, 44 (2005). Modeling the Flow of Complex Fluids Through Heterogeneous Channels.

152. A. J. Wagner and J. M. Yeomans, *Phys. Rev. E*, **59**, 4366 (1999). Phase Separation Under Shear in Two-Dimensional Binary Fluids.

153. J. W. Cahn, *J. Chem. Phys.*, **66**, 3667 (1977). Critical Point Wetting.

154. P. G. de Gennes, *Rev. Mod. Phys.*, **57**, 827 (1985). Wetting: Statics And Dynamics.

155. S. Puri and Y. Oono, *Phys. Rev. A*, **38**, 1542 (1988). Study of Phase-Separation Dynamics by Use of Cell Dynamical Systems. II. Two-Dimensional Demonstrations.

156. M. Bahiana and Y. Oono, *Phys. Rev. A*, **41**, 6763 (1990). Cell Dynamical System Approach to Block Copolymers.

157. A. Shinozaki and Y. Oono, *Phys. Rev. E*, **48**, 2622 (1993). Spinodal Decomposition in 3-Space.

158. A. Briant, *Phil. Trans. R. Soc. Lond. A*, **360**, 485 (2002). Lattice Boltzmann Simulations of Contact Line Motion in a Liquid-Gas System.

159. A. J. Briant, A. J. Wagner, and J. M. Yeomans, *Phys. Rev. E*, **69**, 031602 (2004). Lattice Boltzmann Simulations of Contact Line Motion. I. Liquid-Gas Systems.

160. A. Lamura, G. Gonnella, and J. M. Yeomans, *Europhys. Lett.*, **45**, 314 (1999). A Lattice Boltzmann Model of Ternary Fluid Mixtures.

161. K. Good, O. Kuksenok, G. A. Buxton, V. V. Ginzburg, and A. C. Balazs, *J. Chem. Phys.*, **121**, 6052 (2004). Effect of Hydrodynamic Interactions on the Evolution of Chemically Reactive Ternary Mixtures.

162. R. D. M. Travasso, G. A. Buxton, O. Kuksenok, K. Good, and A. C. Balazs, *J. Chem. Phys.*, **122**, 194906 (2005). Modeling the Morphology and Mechanical Properties of Sheared Ternary Mixtures.

163. C. M. Pooley and K. Furtado, *Phys. Rev. E*, **77**, 046702 (2008). Eliminating Spurious Velocities in the Free-Energy Lattice Boltzmann Method.

164. M. Cates, J.-C. Desplat, P. Stansell, A. Wagner, K. Stratford, R. Adhikari, and I. Pagonabarraga, *Phil. Trans. R. Soc. Lond. A*, **363**, 1917 (2005). Physical and Computational Scaling Issues in Lattice Boltzmann Simulations of Binary Fluid Mixtures.

165. R. Vrancken, M. Blow, H. Kusumaatmaja, K. Hermans, A. Prenen, C. Bastiaansen, D. Broer, and J. Yeomans, *Soft Matter*, **9**, 674 (2013). Anisotropic Wetting and De-Wetting of Drops on Substrates Patterned with Polygonal Posts.

166. L. Moevius, Y. Liu, Z. Wang, and J. M. Yeomans, *Langmuir*, **30**, 13021 (2014). Pancake Bouncing: Simulations and Theory and Experimental Verification.

167. K. Connington and T. Lee, *J. Mech. Sci. Technol.*, **26**, 3857 (2012). A Review of Spurious Currents in the Lattice Boltzmann Method for Multiphase Flows.

168. A. J. Wagner, *Int. J. Mod. Phys. B*, **17**, 193 (2003). The Origin of Spurious Velocities in Lattice Boltzmann.

169. X. Shan, *Phys. Rev. E*, **73**, 047701 (2006). Analysis and Reduction of the Spurious Current in a Class of Multiphase Lattice Boltzmann Models.

170. T. Lee and P. F. Fischer, *Phys. Rev. E*, **74**, 046709 (2006). Eliminating Parasitic Currents in the Lattice Boltzmann Equation Method for Nonideal Gases.

171. T. Seta and K. Okui, *J. Fluid Sci. Technol.*, **2**, 139 (2007). Effects of Truncation Error of Derivative Approximation for Two-Phase Lattice Boltzmann Method.

172. A. J. Briant, A. J. Wagner, and J. M. Yeomans, *Phys. Rev. E*, **69**, 031602 (2004). Lattice Boltzmann Simulations of Contact Line Motion. I. Liquid-Gas Systems.

173. C. M. Pooley, H. Kusumaatmaja, and J. M. Yeomans, *Phys. Rev. E*, **78**, 056709 (2008). Contact Line Dynamics in Binary Lattice Boltzmann Simulations.

174. Q. Li, K. Luo, and X. Li, *Phys. Rev. E*, **87**, 053301 (2013). Lattice Boltzmann Modeling of Multiphase Flows at Large Density Ratio with an Improved Pseudopotential Model.

175. J. Bao and L. Schaefer, *Appl. Math. Model.*, **37**, 1860 (2013). Lattice Boltzmann Equation Model for Multi-Component Multi-Phase Flow with High Density Ratios.

176. A. Fakhari, D. Bolster, and L.-S. Luo, *J. Comput. Phys.*, **341**, 22 (2017). A Weighted Multiple-Relaxation-Time Lattice Boltzmann Method for Multiphase Flows and Its Application to Partial Coalescence Cascades.

177. C. Denniston, E. Orlandini, and J. Yeomans, *Phys. Rev. E*, **63**, 056702 (2001). Lattice Boltzmann Simulations of Liquid Crystal Hydrodynamics.

178. C. Denniston, D. Marenduzzo, E. Orlandini, and J. Yeomans, *Phil. Trans. R. Soc. Lond. A*, **362**, 1745 (2004). Lattice Boltzmann Algorithm for Three-Dimensional Liquid-Crystal Hydrodynamics.

179. D. Marenduzzo, E. Orlandini, M. Cates, and J. Yeomans, *Phys. Rev. E*, **76**, 031921 (2007). Steady-State Hydrodynamic Instabilities of Active Liquid Crystals: Hybrid Lattice Boltzmann Simulations.

180. D. Marenduzzo, E. Orlandini, M. Cates, and J. Yeomans, *J. Non-Newtonian Fluid Mech.*, **149**, 56 (2008). Lattice Boltzmann Simulations of Spontaneous Flow in Active Liquid Crystals: The Role of Boundary Conditions.

181. T. Saw, A. Doostmohammadi, V. Nier, L. Kocgozlu, S. Thampi, Y. Toyama, P. Marcq, C. Lim, J. M. Yeomans, and B. Ladoux, *Nature*, **544**, 212 (2017). Topological Defects in Epithelia Govern Cell Death and Extrusion.

182. H. Chen, B. Boghosian, P. Coveney, and M. Nekovee, *Proc. R. Soc. Lond. A*, **456**, 2043 (2000). A Ternary Lattice-Boltzmann Model for Amphiphilic Fluids.

183. B. M. Boghosian, P. V. Coveney, and P. J. Love, *Proc. R. Soc. Lond. A*, **456**, 1431 (2000). A Three Dimensional Lattice-Gas Model for Amphiphilic Fluid Dynamics.

184. M. Nekovee, P. V. Coveney, H. Chen, and B. M. Boghosian, *Phys. Rev. E*, **62**, 8282 (2000). Lattice-Boltzmann Model for Interacting Amphiphilic Fluids.